$\pi^{\pm}p$ BACKWARD ELASTIC SCATTERING BETWEEN 30 AND 90 GeV/c

by

Paul Anthony Polakos

A Dissertation Submitted to the Faculty of the

DEPARTMENT OF PHYSICS

In Partial Fulfillment of the Requirements
For the Degree of

DOCTOR OF PHILOSOPHY

In the Graduate College

THE UNIVERSITY OF ARIZONA

1 9 8 2

THE UNIVERSITY OF ARIZONA
GRADUATE COLLEGE

As members of the Final Examination Committee, we certify that we have read the dissertation prepared by Paul Anthony Polakos

entitled $\pi^{\pm}p$ Backward Elastic Scattering Between 30 and 90 GeV/c

and recommend that it be accepted as fulfilling the dissertation requirement for the Degree of Doctor of Philosophy.

Bruce R. Barnett	March 12, 1981 Date
Robert L. Thorn	March 12, 1981 Date
	Date
	Date
	Date

Final approval and acceptance of this dissertation is contingent upon the candidate's submission of the final copy of the dissertation to the Graduate College.

I hereby certify that I have read this dissertation prepared under my direction and recommend that it be accepted as fulfilling the dissertation requirement.

Theodore Bowen Dissertation Director	March 12, 1981 Date

STATEMENT BY AUTHOR

This dissertation has been submitted in partial fulfillment of requirements for an advanced degree at The University of Arizona and is deposited in the University Library to be made available to borrowers under rules of the Library.

Brief quotations from this dissertation are allowable without special permission, provided that accurate acknowledgment of source is made. Requests for permission for extended quotation from or reproduction of this manuscript in whole or in part may be granted by the head of the major department or the Dean of the Graduate College when in his judgment the proposed use of the material is in the interests of scholarship. In all other instances, however, permission must be obtained from the author.

SIGNED: Paul Anthony Palakes

ACKNOWLEDGMENTS

I would like to express my deepest appreciation to all those whose help has made this work possible. I regret that the passing of my dear friend and colleague Dr. Robert Kalbach, who was responsible for interesting me in this project initially, makes it not possible to personally thank him. I am deeply indebted to him. I would like to thank Dr. Theodore Bowen of The University of Arizona for his guidance and assitance throughout my graduate career. I also thank Dr. Roy Rubinstein and Dr. Win Baker for inviting me to work with them at Fermilab, and for their help in all phases of this experiment. To all my colleagues at Arizona and Fermilab, especially Dr. Alburt Pifer, Dr. David Eartly, Dr. Arlene Lennox, and Dr. John Klinger go my thanks for their invaluable assistance and the happy memories of working with them. I would like to also thank Jacqueline Ruiz for working so hard far beyond the call of duty in typing this document.

Finally I thank my wife, Ellen and my children Noelle and Nathan, for enduring the many lost evenings and weekends spent bringing this work to fruition.

To my parents, for the love and encouragement they have always given me, I owe all. To them, I dedicate this work.

TABLE OF CONTENTS

		Page
	LIST OF ILLUSTRATIONS	v
	LIST OF TABLES	vii
	ABSTRACT	viii
1.	INTRODUCTION	1
2.	EXPERIMENTAL METHOD	9
	a. Beam	10
	b. Liquid Hydrogen Target	15
	c. Forward Spectrometer	16
	d. Backward Spectrometer	20
	e. Trigger Logic	23
3.	DATA ANALYSIS	27
	a. Reconstruction	27
	b. Event Selection	33
	c. Inelastic Background	39
	d. Corrections	41
4.	RESULTS	46
	a. General Features	46
	b. Discussion	53
	APPENDIX A: FAST LOGIC	64
	a. Beam Logic	64
	b. Slow Arm Logic	65
	c. Fast Arm Logic	66
	d. Gating Logic	66
	REFERENCES	72

LIST OF ILLUSTRATIONS

Figure		Page
1.	Baryon Exchange Diagrams for π^+p, π^-p Elastic Scattering	4
2.	Schematic Diagram of Fermilab M6 Beam Line	11
3.	Experimental Layout	14
4.	Backward Spectrometer Layout	21
5.	Block Diagram of Fast Logic	24
6.	x_π Distribution	35
7.	Δp_x Distribution	36
8.	Δp_y Distribution	37
9.	Δx_{p6} Distribution	38
10.	Experimental Acceptance	44
11.	Backward π^+p Elastic Scattering Differential Cross-Sections	47
12.	Backward π^-p Elastic Scattering Differential Cross-Sections	48
13.	Slope of Backward Elastic Peak as a Function of Laboratory Momentum	50
14.	Momentum Dependence of Elastic Differential Cross-Section at u = 0	51
15.	Effective Regge Trajectory for π^-p Backward Elastic Scattering	58
16.	Effective Regge Trajectory for π^+p Backward Elastic Scattering	59
17.	Comparison of the Results at 50 GeV/c for $d\sigma/du$ for π^+ and π^- Backward Elastic Scattering with the Predictions of a Simple Regge Model	60

LIST OF ILLUSTRATIONS--Continued

Figure Page

18. Detailed Diagram of Beam Logic 68

19. Detailed Diagram of Slow Arm Logic 69

20. Detailed Diagram of Fast Arm Logic 70

21. Detailed Diagram of Gating Logic 71

LIST OF TABLES

Table		Page
1.	Summary of Data Taken for π^+ and π^- Running from 30-90 GeV/c	28
2.	π^+p Backward Elastic Differential Cross-Sections	60
3.	π^-p Backward Elastic Differential Cross-Sections	61
4.	Results of Exponential Fits of the Backward Peaks	62

ABSTRACT

Measurements of the differential cross sections for backward π^+p and π^-p elastic scattering have been made for incident pion momenta between 30 and 90 GeV/c in the angular range $0<-u<0.5(\mathrm{GeV/c})^2$ $[168° < \theta_{cms} < 180°]$. The experiment was performed in a high momentum, high resolution hadron beam at the Fermi National Accelerator Laboratory. Interactions were produced in a liquid hydrogen target placed in the beam, and the scattering angles and momenta of the recoil pion and proton were measured in separate magnetic spectrometers. Backward elastic events were identified as those which satisfied the correct kinematic constraints.

The angular distributions of the differential cross section are similar to those observed in the data of previous experiments below 20 GeV/c. A narrow backward peak at $u = 0$ with a sharp dip at $-u \simeq 0.15$ $(\mathrm{GeV/c})^2$ and a broad second maximum between $-u \simeq .25$ and $.45$ $(\mathrm{GeV/c})^2$ are observed in the π^+ cross sections for incident pion momenta of 30 and 50 GeV/c; evidence for similar structure is also seen at 70 GeV/c. On the contrary, the π^- cross sections have a much broader backward peak with no evidence of a dip.

The data are consistent with the parameterization given by a simple Reggeized baryon exchange model. It is supposed that the scattering may be explained by the exchange of only two specific trajectories; the Δ_δ for $\pi^- p \to p\pi^-$, the Δ_δ and N_α for $\pi^+ p \to p\pi^+$. As is given by this model, the momentum dependence of the differential cross-section, $d\sigma/du$ for fixed u, may be parameterized with the form $p_{lab}^{-n(u)}$. The values $n^+ = 2.31 \pm 0.07$ and $n^- = 2.08 \pm 0.06$ are obtained for n at u = 0 for π^+ and π^- scattering respectively.

CHAPTER 1

INTRODUCTION

This dissertation reports the results of an investigation of the backward elastic scattering of pions on protons at high energies. The data presented are the results of an experiment at Fermilab designed specifically to look at elastic interactions where pions are scattered in the CMS angular range $168° \lesssim \theta_{cms} \lesssim 180°$ $[0 \lesssim -u \lesssim 0.5\ (\mathrm{GeV/c})^2]$ for incident pion momenta from 30 to 90 GeV/c. After describing the experimental method and data analysis procedure, the results are given and compared to existing data and to theoretical models of the process.

Interest in backward elastic scattering was spurred in 1965 by the report[1] of an accumulation of events scattered at 180° when 4 GeV/c positive pions interacted with the protons in a liquid hydrogen bubble chamber at the CERN Proton Synchrotron. Other experiments [2-9] followed, firmly establishing the existence of a sharp peak in the elastic cross section at 180° for both π^+p and π^-p interactions for incident pion momenta from $\sim$ 2 to 18 GeV/c. The results were striking. The well known forward peak of the differential cross section was successfully described by optical and Regge pole models involving pomeron and meson exchanges, which also

predicted a decrease in cross section with increasing 4-momentum transfer squared t (hence increasing scattering angle). The peak in the backward direction, at $t = t_{max}$, suggested some other dynamical process to be responsible for scattering in this angular region.

The data below 18 GeV/c are found to have a natural division at $\sim$ 5 GeV/c. Below this momentum, the differential cross section at 180^0 varies erratically with energy, showing peaks and dips at various momenta. The correlation of these irregularities at energies corresponding to the masses of known baryon resonances supports the contention that a major contribution to the backward cross section comes from resonance formation in the s-channel. That is, if the isobar production reaction $\pi^{\pm}p \rightarrow N^{*}(\Delta)$ is followed by decay of the isobar into the original particles, $N^{*}(\Delta) \rightarrow p\pi^{\pm}$, such a process would be indistinguishable from backward scattering. The reaction with isobar production has an energy dependence which is resonant in character, and this is directly revealed in the backward elastic cross-section. Generally, good fits to the data are obtained if one assumes a scattering amplitude written as the sum of a Breit-Wigner resonance amplitude and a non-resonant background, usually written in terms of a Regge amplitude[6].

Above 5 GeV/c, the resonant contribution subsides and up to $\sim$ 18 GeV/c the data show several characteristic features:

(1) The elastic differential cross-section at 180^0 for π^+p interactions is larger than for π^-p interactions. At 6 GeV/c, the ratio π^+/π^- is $\sim$ 4.

(2) The momentum dependence for the differential cross section at 180° falls smoothly as p_{lab}^{-n} where n = -2.0 for π^-p and n=2.7 for π^+p scattering.

(3) For fixed incident momentum, the dependence of the differential cross section $d\sigma/du$ on u near u=0 is of the form e^{Bu} [where $u=-2q^2\ (1+\cos\theta^*)$; q=CMS momentum; θ^*=CMS pion scattering angle].

(4) for π^+p scattering, a sharp dip in $d\sigma/du$ is observed near u=-.15 $(GeV/c)^2$. No such dip is observed for π^-p scattering.

Although several optical models are capable of producing peaks in the backward hemisphere[10-11], none can satisfactorily explain the observed differences in magnitude and shape of the π^+ and π^- backward differential cross sections. The best fits to the data were obtained with a model based on Reggeized baryon exchange [12-13].

Within the model, the backward elastic interaction is viewed as a quasi-inelastic process in which the incident pion is converted into a target proton and continues in the

same direction with a minimal change in momentum. In the interaction, the appropriate quantum numbers (baryon number, isospin) are exchanged in the crossed (u) channel with small 4-momentum transfer. The appropriate diagrams for $\pi^{\pm}p$ scattering are shown in fig. 1. Hence, the apparently violent collision [t=s] is treated as a soft, peripheral process in the u-channel. Much in the same way that the peripheral exchange of mesons the t-channel leads to a peak in forward direction, so does the peripheral exchange of baryons in the u-channel lead to a backward peak.

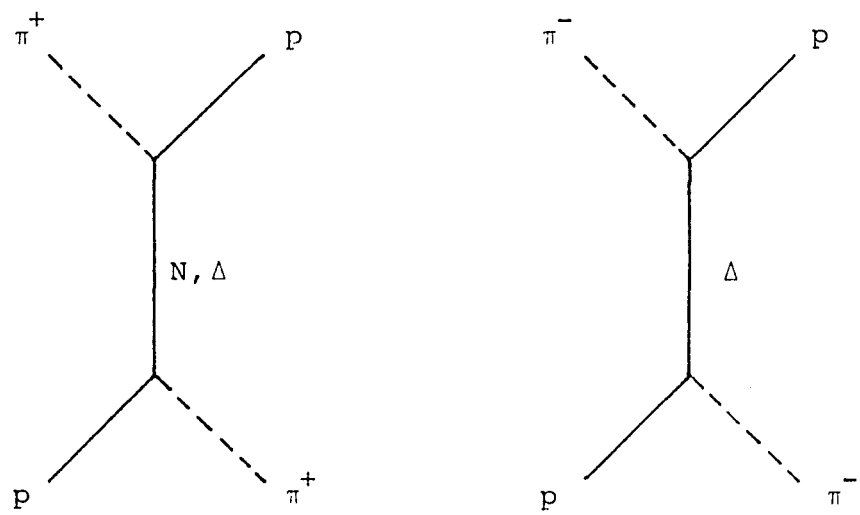

Figure 1. Baryon exchange diagrams for π^+ and π^- proton backward elastic scattering.

This hypothesis is well verified in a variety of other interactions, and it seems relatively well established that for CMS energies above the resonance region, when the exchange of a known baryon would lead one to predict a backward peak then, and only then, is one observed[14].

In Regge theory, an interaction is mediated by the exchange of a reggeon, an assembly of particles with definite quantum numbers (baryon number, isospin, parity) except spin, which varies continuously with the four momentum transfer squared (u). The functional relationship between spin and u, known as the Regge trajectory, is not predicted by the theory; in the simplest models it is assumed to be linear (as suggested by its form in the physical mass region of the Chew-Frautschi plots). The scattering amplitude is written as:[15]

$$M = F(u) \frac{1 + i\tau e^{-i\pi\alpha(u)}}{\cos \pi\alpha(u)} \quad \frac{s}{s_0}^{\alpha(u)-1/2}$$

- $F(u)$ - real function of u
- $\alpha(u)$ - Regge trajectory
- τ - ± 1 signature of trajectory

which gives a differential cross section of the form:

$$\frac{d\sigma}{du} \sim \frac{1}{s}|M|^2 = f(u) \quad \frac{s}{s_0}^{2\alpha(u)-2}$$

Hence, it is predicted that $d\sigma/du$ for fixed u varies as a power of s, which at high energies means a power of P_{lab}.

For π^+p scattering, the amplitude can contain contributions from the N_α and Δ_δ trajectories (associated with the nucleon, and 3,3 resonance respectively)(*). In π^-p scattering, only the Δ_δ contributes. The strong differences in magnitude and angular distribution of the π^+p and π^-p cross sections have been interpreted as evidence that the Δ_δ contribution to π^+p scattering below 20 GeV/c is small. Under this assumption, a fit to the data with a conventional Regge model using linear trajectories was performed and found in good agreement with extrapolations of linear fits to known baryon resonance masses for $u < 0$. The sharp dip in the π^+p angular distribution was attributed to the vanishing of the signature term, $1 + i\tau e^{-i\pi\alpha(u)}$, of the N_α amplitude at $\alpha_N(u)=-1/2$. Because of the opposite signature of the Δ_δ trajectory, no dip at $\alpha(u)=-1/2$ is predicted in π^-p scattering; nor is one observed.

(*) The exchange of the N_γ trajectory is also possible and may contribute to the scattering amplitude. However, in the simple Regge model, this contribution is assumed to be small. For further discussion, see Chapter IV.b.

Subsequent results from polarization experiments and backward charge exchange ($\pi^- p \to n\pi^0$) experiments, which also may exchange N and Δ trajectories, could not be explained by this conventional Regge model. More sophisticated models, incorporating additional trajectories, absorption and cuts, were proposed to fit the data [16-18]. However, for $\pi^{\pm}p$ scattering near $u \approx 0$ it was believed that the conventional model would remain approximately valid.

Using this model, one can make definite predictions on the behaviour of the cross sections with increasing energy. If one writes the amplitudes as[19]:

$$f^+ = 2/3\ N + 1/3\ \Delta$$

$$f^- = \Delta$$

where N, Δ are the amplitudes for N_α and Δ_δ exchange respectively, then since the N_α trajectory lies below the Δ_δ, the N_α amplitude will fall more rapidly than the Δ_δ with increasing energy. Hence it is expected that asymptotically both scatterings should be dominated by Δ_δ exchange. Specifically, the π^+p angular cross-section $d\sigma^+/du$ at $u = 0$ should become $\sim 1/9\ d\sigma^-/du$ at high incident momentum, contrary to the situation at lower momenta. From an extrapolation of low momentum results one would expect the cross sections to cross at $\sim$ 50 GeV/c. It is also predicted that the dip in the π^+p angular distribution will disappear at high momentum, gradually being filled in by the contribution from

the Δ_0 exchange. Eventually the π^+ angular distribution should become similar to the π^-.

The first results above 18 GeV/c came from experiments performed at Serpukhov by Babaev and co-workers[20-21] during the first half of the 1970's, where they studied the reactions $\pi^- n \to n\pi^-$ (isotopically equivalent to $\pi^+ p \to p\pi^+$) and $\pi^- p \to p\pi^-$ at $\sim$ 25 and 38 GeV/c. For the former reaction, they measured $d\sigma^+/du$ at u = 0 to be about a factor 3 larger than was expected from an extrapolation of low momentum results using the expected $p^{-2.7}$ momentum dependence. The angular distribution also remained sharply peaked, as at lower momenta. In the latter reaction, although the magnitude of the cross section $d\sigma^-/du$ at u=0 was consistent with Regge predictions, the angular distribution became much more peaked near u=0. These results could not be explained by the conventional Regge model and indicated the possible existence of new (non-Regge) terms in the scattering amplitude. It was argued that the effect of such terms would not be seen at lower energies due to small couplings, but would have a lesser momentum dependence than Regge terms and would asymptotically dominate over them. New models were proposed along these lines [22-24].

This experiment at Fermilab was performed to test the theoretical models to the highest energy practical, and to cover the momentum range of the Serpukhov experiments again.

CHAPTER 2

EXPERIMENTAL METHOD

The elastic interactions were produced by directing a pion beam of known momentum onto a liquid hydrogen target. The scattering angles and momenta of the recoil pion and proton were measured in separate magnetic spectrometers. Each spectrometer consisted of an analysis magnet to disperse momenta, with scintillation counter hodoscopes and multiwire proportional chambers (MWPC's) on either side to determine particle trajectories. A threshold Cerenkov counter was placed in the forward spectrometer to identify the forward scattered particle as a proton. The counter hodoscopes provided a fast, albeit crude, momentum-angle measurement for each particle. An electronic comparison was made between the forward and backward hodoscopes, and any event whose correlation was close to that expected for an elastic scatter was selected as an elastic candidate at the trigger level. For these events, the precise trajectory information from the MWPC's and other spectrometer instrumentation was saved on magnetic tape for more detailed off-line analysis. A description of the beam line and spectrometer systems is given below.

a. Beam

The pions for experimental use were produced by steering a 400 GeV/c proton beam, extracted from the Fermilab Proton Synchrotron, onto a 20.3 x 0.05 x 0.05 cm beryllium target. Secondary particles produced at a 2.5 mr horizontal angle were collected, momentum analyzed and identified in a 420 meter long beam line, and directed onto a liquid hydrogen target. A schematic layout of the beam transport components which form the M6 beam line at Fermilab is shown in fig. 2.

The M6 beam is a high momentum, high resolution beam line with three stages and three foci. Following the target is a set of septum magnets and collimators which define the angular acceptance of the beam line. The first set of quadrupole magnets, Q_1Q_2, form a focusing doublet which produces a parallel beam which is then dispersed in momentum by the main bend dipoles B1. Particles of the desired momentum are focused horizontally and vertically at the first focus by the second quadrupole doublet, Q_3Q_4. At this focus the beam has a momentum dispersion of approximately 6 cm/(% $\Delta p/p$). The momentum acceptance of the beam is defined by the movable jaws of the $\Delta p/p$ collimator. During the experiment the aperture of this collimator was varied from $\sim$ 1-3 cm depending on momentum to maintain the desired flux on the liquid hydrogen target.

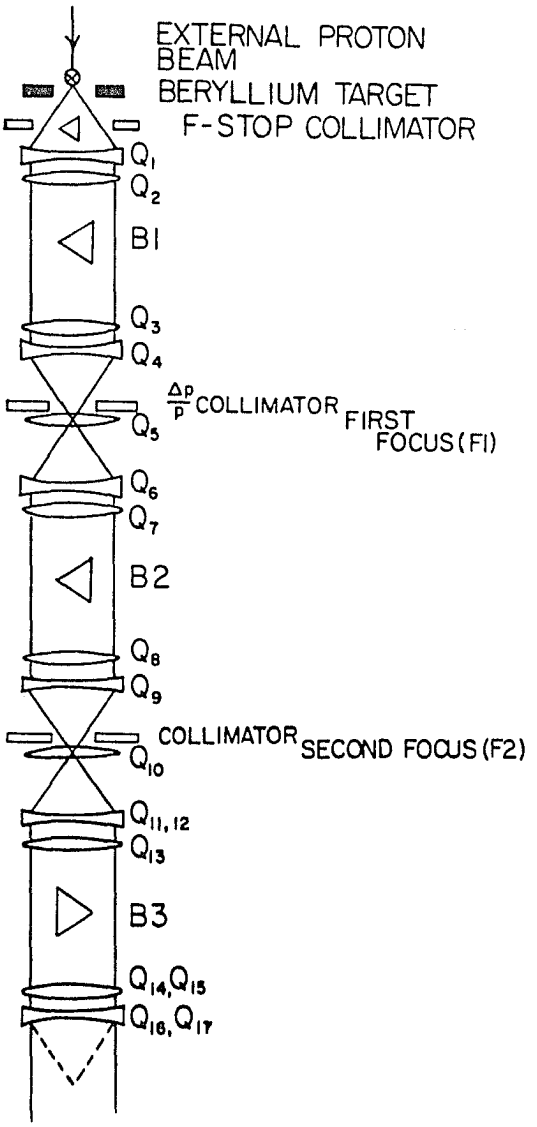

Figure 2. Schematic Diagram of Fermilab M6 Beam Line.

A field lens consisting of a single horizontally focusing quadrupole, Q_5, is also located at the 1st focus to minimize vignetting.

A similar transformation, point to parallel, bend, parallel to point, is repeated in the second section. Momentum dispersion at the 2nd focus is 4.442 cm/(%$\Delta p/p$). Horizontal and vertical collimators are used there to minimize beam halo. Another single horizontally focusing quadrupole, Q_{10}, acts as a field lens.

In the third stage of the beam, the point to parallel transformation is performed by the quadrupole triplet, Q_{11}, Q_{12}, Q_{13}. Dipole bend string B3 recombines momentum by reversing the dispersion introduced by B2 and B3. The quadrupoles Q_{14-17} refocus the beam wherever desired. For this experiment, a parallel beam at the liquid hydrogen target was required, therefore this final focusing procedure was not performed.

The beam was defined for trigger purposes by a beam telescope consisting of three plastic scintillation counters. (B1, B2, A1 in fig. 3). The dimensions of these counters were:

Counter	Size (cm)	Thickness (cm)
B_1	3.8 cm dia	0.64 cm
B_2	3.8 cm dia	0.64 cm
A_1	20.x20. cm w/3.8 cm hole	0.64 cm

A fast logic coincidence/anticoincidence between $B_1 B_2 \overline{A_1}$ made it possible to tag a beam particle while eliminating those which interacted upstream.

Partial identification of beam particles was provided by an 18 meter long He gas threshold Cerenkov counter located in the third section of the beam line. With its pressure adjusted just above pion threshold, it tagged particles of a pion mass or less, thereby eliminating triggers caused by protons or kaons. Remaining minority particles in the beam (muons and electrons) were measured at every beam momentum and polarity. The percentage of muons was determined by measuring beam transmission through a 4.5 meter Fe beam stop, and found to vary between 1% and 2% depending on beam momentum. Electron contamination was measured with a 13 x 13 x 25 cm lead glass shower counter. The signals from a photomultiplier optically coupled to the block were digitized and properly normalized provided a direct measure of the fraction of electrons in the beam. This fraction varied from $\sim$ 10% at 30 GeV/c to a negligible amount above 70 GeV/c.

Beam size at the hydrogen target was approximately 3.8 cm in diameter. It had a divergence of $\sim$ ±0.3 mrad. and a nominal momentum spread of ±0.2%. Approximately 1.5 x 10^6 beam pions were uniformly received per 1 second synchrotron spill. Since the proton beam circulating in the

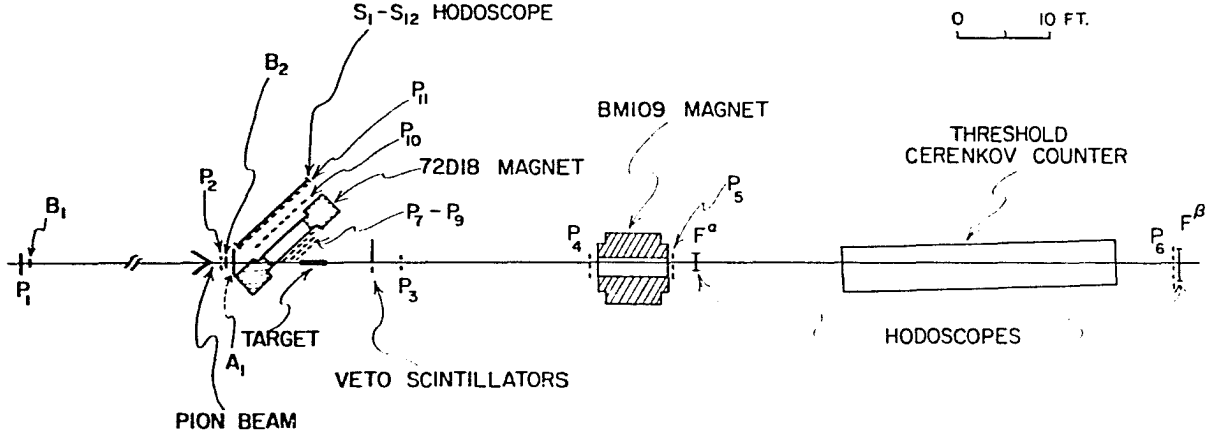

Figure 3. Experimental Layout.

synchrotron was not debunched prior to extraction, the secondary pion beam exhibited the RF structure impressed during acceleration. Pions therefore were confined to arriving in buckets, each separated by approximately 19 nanoseconds; roughly 1 bucket in 35 was occupied.

A 32 element scintillation counter hodoscope was placed at the 2nd focus (F2 in fig. 2) to accurately define the momentum of an incident pion. Each element measured 3 mm wide and overlapped its neighbour by 1/3 giving a spacial resolution of 1 mm. At F2, this translated to a momentum resolution of ±0.024%. Two sets of wire proportional chambers located 22 and 3 meters upstream of the liquid hydrogen target provided directional and positional information of the incident beam. Each set contained both x and y planes with wirespacings of 2mm; angular resolution of the arrangement was ±0.06 mrad.

b. Liquid Hydrogen Target

The target consisted of a cylindrical vessel, 1 meter long and 7.5 cm in diameter, constructed of 0.25 mm mylar. The vessel was wrapped in ∿ 40 layers of 6.4 mm aluminized mylar to minimize radiative heat absorption, and suspended in an evacuated target enclosure. The necessary plumbing connections were provided between the vessel and a hydrogen liquification system to allow easy filling and proper venting of the target. The target enclosure had an

unusually large exit window constructed of 0.4 mm mylar spanning the entire length of one side and both ends. This feature was necessary to accomodate the large angular range of the scattered pions and the length of the target. Filled with liquid hydrogen, the target represented approximately 0.1 absorption lengths.

All sides of the target enclosure, excluding the exit window, were covered by veto counters to improve rejection of inelastic interactions. Additional veto counters were also judiciously located downstream (see figs. 3,4).

c. Forward Spectrometer

Trajectory and momentum information on the forward going proton was provided by four sets of multiwire proportional chambers (MWPC's) located on either side of an analysis magnet as shown in fig. 3. The two chambers (P3,P4) located between the target and the magnet consisted of one x and y plane each; the two behind the magnet (P5,P6), one x plane each. Lateral wire spacing for all planes was 2 mm and the chambers were adequately dimensioned not to be aperture limits.

Momentum dispersion was provided by the magnetic field of one or two standard Fermilab BM109 analysis magnets. Each magnet had a gap of 6" x 24", pole length of 72" and equipped with conventional coils could produce a maximum field integral of 1450 kG-in.

So that resolution and acceptance could be maintained over the desired momentum range from 30 to 90 GeV/c, the length of the spectrometer was approximately scaled. In total, two layouts were used. In the first layout, for data taking at ±30 and ±50 GeV/c, the overall length was 30 meters with a single analysis magnet located 11 meters from the target. The magnetic field integral was held at a constant 1337 kG-in for both incident momenta, which provided a momentum resolution $\Delta p/p^2 = \pm 2\times10^{-4}$ $(GeV/c)^{-1}$. The scattering angle resolution, $\Delta\theta$, of this arrangement was ±0.34 mrad.

In the second layout, used for additional running at -50 GeV/c, and for running at ±70 and -90 GeV/c, the overall length was increased to 60 meters. Two analysis magnets were necessary to obtain the desired momentum resolution and were located a distance of 31 meters from the target. The magnet field was scaled with momentum to provide the same resolution at the three momenta. To minimize the detrimental effects of multiple scattering on the spectrometer resolution, helium-filled drift spaces were provided before and after the analysis magnets where space allowed. This geometry had momentum ($\Delta p/p$) and scattering angle resolutions of ±0.4% and ±0.110 mrad. respectively. For both layouts, the acceptance was well matched to that of the backward spectrometer, both approximately covering the same CMS angular range for backward elastic interactions.

The forward spectrometer contained additional instrumentation designed to quickly provide information on the forward scattered particle and be used in forming the trigger. A scintillation counter telescope array, consisting of two hodoscope planes of eight elements each, was located beyond the analysis magnet (F_α, F_β in fig. 3) to provide a crude determination of the scattering angle and momentum of the particle. The elements of each hodoscope were physically placed such that a simple coincidence between a given element in F_α and the corresponding element in F_β indicated a particle with a scattering angle momentum combination expected for an elastic scatter. The approximate resolution of a pair of elements was $\sim$5.0 ($\sim$ 0.3) mrad. for the low (high) momentum geometries corresponding to a momentum resolution, $\Delta p/p \simeq \pm 13\%$. The information from this telescope, together with that from the backward spectrometer hodoscope provided the kinematic constraints on a trigger which heavily favoured elastic scattering.

A 1.5 meter diameter, nine meter long gas Cerenkov counter was also located in the downstream half of the forward spectrometer. Set just below the threshold of the highest momentum proton expected from an elastic scatter, it was used to veto any particle not a proton which otherwise satisfied the trigger requirements. The large aperture was necessary to cover the entire angular range of the

elastically scattered protons. The counter found its greatest usefulness in the π^+ running, where the peripherally scattered π^+ kinematically closely resembles the proton from a backward elastic scatter. In this case, the trigger rate was typically reduced a factor 70 by including the Cerenkov counter in veto. For π^- running, a forward scattered π^- followed a vastly different trajectory from a proton beyond the analysis magnet, thereby increasing the efficiency of the kinematic trigger requirements. Inclusion of the Cerenkov counter reduced the trigger rate by 1.5 in this case.

The Cerenkov light produced in the counter was focused by four spherical mirrors mounted at the downstream end onto the 1.5" photocathode of an RCA C31000-M photomultiplier. Particles exiting the counter had to traverse the one-inch glass from which the mirrors were made, therefore the counter was placed as close as possible to the final MWPC to minimize position measurement errors caused by multiple coulomb scattering and interactions in the glass.

d. Backward Spectrometer

Because the backward pion momentum is much lower than the forward protons, the backward spectrometer was of more modest proportions, being 2.5 meters overall in length. Its position, on an axis rotated 135^0 from the incident beam direction about the center of the hydrogen target, was determined by a Monte-Carlo program as providing the largest geometrical acceptance for the given magnet aperture (fig. 4). To minimize instrumental uncertainties, it was designed to cover the desired center of mass angular range ($168° \leq \theta_{cms} \leq 180°$) without a change in geometry. Since the backward scattered pion kinematics are relatively independent of incident momentum in the range covered by this experiment, the same layout could be used for all momenta.

As in the forward spectrometer, MWPC's were used to define particle trajectories on either side of the analysis magnet. Before the magnet, lateral track position was determined by 2 planes of vertical wires of 2 mm spacing, separated by 13 cm; vertical position by 3 planes of horizontal wires also spaced by 2 mm and separated by 13 cm and 10 cm. The chambers were aligned and fixed in a cradle which was attached to the front face of the magnet. This compact configuration permitted close placement of the

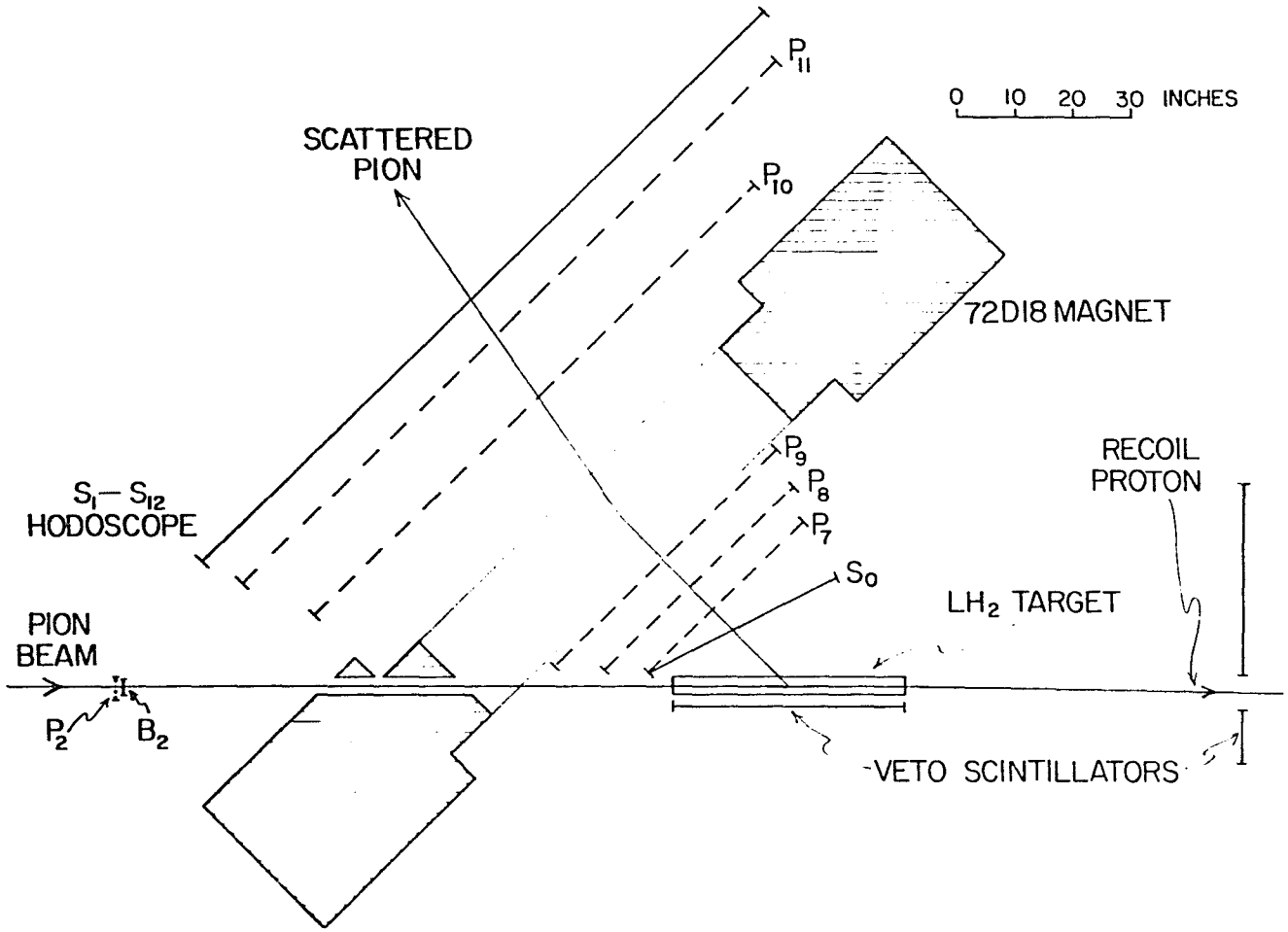

Figure 4. Backward Spectrometer Layout.

analysis magnet to the target thereby maximizing acceptance. The analysis magnet aperture was 183 cm x 46 cm with a pole length of 46 cm. The central field developed was 4.2 kG giving an effective field integral of 126 kG-inch. The field orientation depended on beam polarity and was selected such that the backward elastically scattered pion was always bent away from the incident beam axis. Due to the proximity of the magnet and target, it was necessary to cut a channel in the return iron to allow the incident beam to pass through. The field in this channel introduced a slight deflection in the incident beam direction which was measured during calibration runs and corrected for in the analysis. Behind the magnet, only the horizontal track projection was measured, using two planes of vertical wires. Wire spacing in the planes was 2 mm with adjacent wires joined together, yielding an effective spacing of 4 mm. The distance between planes was $\sim$ 40 cm. To accomodate the large angular range of the back scattered pions in the Lab, the vertical planes each consisted of several individual chambers positioned side by side; two in the first plane, three in the second. The chamber frames were overlapped to minimize holes in the acceptance. Monte-Carlo calculation showed this effect to be smeared in u due to the finite target length; the acceptance was corrected accordingly. The sensitive area of all wire planes was sufficient not to be aperture limits.

Located behind the final MWPC plane was the pion trigger hodoscope (S_1-S_{12} Hodoscope in fig. 4). It consisted of 24 scintillation counters 11.5" wide x 12" high arranged in a 2 high by 12 wide matrix. The pion position measured by this hodoscope gave approximate information on the pion momentum and scattering angle (assuming it to be elastic). This information was then used with that from the forward spectrometer telescope in making the trigger decision. The time between beam arrival and the firing of a particular hodoscope element was digitized and saved for each event. This information proved useful in eliminating accidental triggers not originating in the target in the off-line analysis.

e. Trigger Logic

The fast logic system was designed to rapidly identify those events in which a pion entered the target, a recoil particle was detected in the backward spectrometer and a proton passed through the forward spectrometer with the requirement that the trajectories of both particles (as determined by the trigger hodoscopes) were consistent with those expected for an elastic event. A block diagram of the logic is given in fig. 5. A detailed diagram is given in Appendix A.

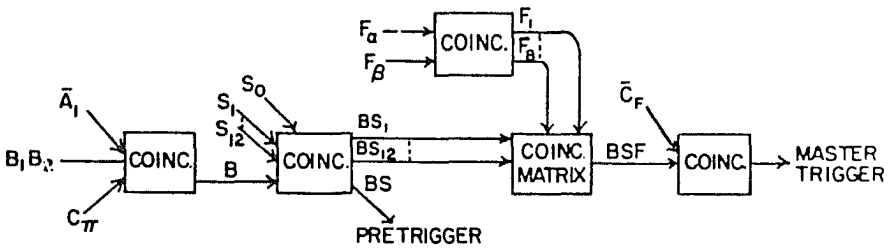

Figure 5. Block Diagram of Fast Logic.

A beam pion was identified by the beam telescope as the coincidence $B=B_1B_2\overline{A_1}C\pi$. To minimize background in the MWPC's, a pion arriving at time t_o was accepted only if it was not accompanied by a second during the time interval $t_o \pm 25$ ns. A signal from the S_o counter and an element of the S-hodoscope at the correct time following B_1 defined as $BS=B.S_o\cdot(S_1+S_2+\ldots S_{12})$, indicated that a particle emerged from the target and passed through the backward arm. The BS signal was used as a pretrigger, which began an event cycle that temporarily disabled the experiment and stored the MWPC and S-hodoscope information in latches until the signals from the forward hodoscopes and Cerenkov counter were received and processed. The coincidences BS_1, $BS_2 \ldots BS_{12}$ were also formed and stored in delay lines for later use in forming the final trigger.

Typically 1 beam pion in 2000 resulted in a BS pretrigger.

Following a delay a ∿400 ns, the forward hodoscope signals were received and the coincidences $F_i = F_{\alpha i} \cdot F_{\beta i}$ (i=1,8) were formed. At this point, the kinematic constraints were imposed. The signal BSF, defined as:

$$BSF = \Sigma BS_i A_{ij} F_j \quad i = 1,12;\ j = 1,8$$

where A_{ij} = 8 x 12 matrix of 0's and 1's

was formed in a hard wired coincidence matrix which described the correlation between elements of the forward and backward hodoscopes for backward elastic events. This correlation followed directly from 2-body elastic kinematics and was determined by computer simulation of elastic events in the apparatus. A BSF signal thus indicated that an event had a hodoscope hit pattern characteristic of an elastic event. In reality, such patterns resulted not only from true backward elastic scatters, but also from nearly elastic inelastic scatters and interactions occurring upstream of the liquid hydrogen target. The latter sources were the most prolific.

The final coincidence, MASTER TRIGGER = $BSF \cdot \overline{C_F}$ ensured the forward particle was a proton and selected the event as a possible elastic event to be saved. The data acquisition computer was notified, and a readout cycle began

transferring the event data stored in the latches and scalers to the computer memory and eventually to magnetic tape. Upon completion of the transfer, the event cycle ended with the clearing of the latches and the appropriate scalers and the reenabling of the experiment. An entire event cycle took approximately 10 milliseconds.

Any BS pretrigger which was not followed by the appropriate signals from the forward counters resulted in the clearing of all temporarily stored data and the prompt reenabling of the experiment without computer readout. The deadtime thus introduced was < 2μsec. Approximately 99% of the pretriggers fell into this category.

Approximately 10 MASTER TRIGGERs were generated for each beam spill of 1.5×10^6 pions.

During the experiment, the outputs of various counters and coincidences were counted on scalers and used as diagnostic checks that the entire apparatus was functioning properly. The total number of pions incident on the liquid hydrogen target during the time the experiment was enabled, as defined by the beam telescope, was scaled at each momentum and used to normalize the final differential cross-sections.

CHAPTER 3

DATA ANALYSIS

The data from this experiment were analyzed on the Fermilab central computers (CDC-6600). The analysis procedure for each event included the geometrical reconstruction, during which time many obviously non-elastic events were excluded, followed by the construction of several kinematic variables which were a measure of how near to elastic the event was. Elastic events were finally selected by making the appropriate cuts on these kinematic variables. Since the cross sections, and hence statistics, were small, particular attention was given to making the analysis program as efficient as possible in extracting elastic events from the data. A summary of the data acquired and analyzed during the experiment is given in Table 1. A detailed description of the various steps in the data analysis follows.

a. Reconstruction

The first stage of the analysis began with the geometrical reconstruction of the event in the backward spectrometer. Tracks were first reconstructed in x projection in front and beyond the analysis magnet. For this to be possible, it was required that at least 3 of the 4 MWPC x planes in the backward arm recorded $\geq$ 1 hit; with less

Table 1. Summary of Data Taken for π^+ and π^- Running from 30-90 GeV/c.

Incident Particle	Momentum (GeV/c)	Number of Pions on Target	Number of Triggers	Number of Elastic Events
π^+	30	25.5×10^9	130×10^3	100
π^+	50	45.4×10^9	263×10^3	62
π^+	70	49.6×10^9	621×10^3	14
π^-	30	33.7×10^9	256×10^3	142
π^-	50	88.6×10^9	271×10^3	121
π^-	70	58.3×10^9	305×10^3	31
π^-	90	43.0×10^9	233×10^3	13

information the event could not be analyzed. Since the MWPC's were less than 100% efficient, it was possible for a pion to pass through the four planes without having all four register a hit. Requiring three of four planes made it possible to obtain good reconstruction efficiency and still extract the desired kinematic information. Given the efficiencies of the chambers, > 95% of the pions from elastic interactions would have trajectories which could be reconstructed under this premise. Events were divided into two groups: (i) those in

which all 4 x-planes recorded at least one hit, and (ii) those in which only 3 of 4 x-planes recorded hits. The method used to construct tracks depended on which category an event fell into.

For events in group (i), a track was formed by joining with a straight line a hit in one x-plane with a hit in the other on the same side of the analysis magnet. In the situation where a plane had more than one hit, all combinations of hits were used to produce a set of tracks. This procedure was used to reconstruct tracks on both sides of the analysis magnet, thus yielding two sets of tracks. To reduce the number of tracks which did not correspond to true charged particle trajectories (combinatorial background), a track behind the analysis magnet was accepted as legitimate only if it extrapolated to an S-hodoscope element which was recorded as being hit. Other tracks were deleted. If in this way all tracks were deleted, it was assumed that one of the planes failed to record a true hit but contained spurious accidental hits. The event was then reclassified into group (ii) and reconstructed as such.

The same procedure, pairing hits between two planes, was also used to generate tracks for events in group (ii), however, in this case it was possible on only one side of the magnet (the side on which both x-planes recorded hits). To produce tracks on the opposite side, the tracks were propagated through the magnetic field and fit to a hit

recorded in one of the x-planes on the opposite side, by varying the curvature (momentum) of the track in the field region. All possible combinations were tried and again only those tracks behind the magnet which extrapolated to a S-hodoscope element which was hit were considered valid.

Either procedure produced two sets of tracks, one before and one after the magnet. Tracks from each set were paired with the requirement that they meet within the magnet aperture, and the momentum calculated. The event was required to have a track pair that pointed back to the liquid hydrogen target, had the correct sign momentum, and had the proper time of flight from the target to the S-hodoscope. A data summary tape was generated on which events meeting these criteria were saved for further analysis. This first stage analysis eliminated $\sim$ 90% of the raw triggers and rapidly reduced the data sample to a more manageable size.

In the second stage of the analysis, incident beam tracks and tracks in forward spectrometer were reconstructed in both x and y projections. For the beam tracks, information from both beam chambers was used if available. If the P_1 chamber failed to record a hit because of inefficiency the positional information from the P_2 chamber was used and the nominal beam direction was assigned to the track. Negligible error was introduced using this procedure owing to the small divergence of the beam. The

beam tracks were extrapolated through the channel in the backward spectrometer analysis magnet, their x slope properly adjusted for the slight deflection introduced in the channel (mentioned earlier), and coupled with a reconstructed track from the backward spectrometer. The projected backward pion scattering angles, θ_x^π and θ_y^π, and the target vertex coordinates were then calculated.

A kinematics program used the incident pion momentum and the backward scattering angle to predict the momentum of the backward pion and the scattering angle and momentum of the forward proton assuming elastic kinematics. The quantity

$$x_\pi = \frac{p_\pi - p'_\pi}{p_\pi \cdot p'_\pi}$$

was calculated, where p_π, (p'_π) is the measured (predicted) pion momentum. This quantity, a measure of the discrepancy of the true pion momentum from that expected of an elastic scatter at the same angle, has the same functional dependence on momentum as the momentum resolution does. Hence, the width of the distribution of elastic events in x_π is constant for all pion momenta, allowing the final elastic cut on this variable to be the same for all scattering angles.

The projected scattering angles of the proton, θ_x^{pr} and θ_y^{pr}, were determined by reconstructing tracks in the first half of the forward spectrometer using the MWPC

information and the reconstructed target vertex as an additional constraint. In order not to lose events due to any inefficiency in P_3, this chamber was not required for track reconstruction but the information from it used if available. In those cases where the P_4 chamber did not record a hit, tracks were generated from the P_5 chamber extrapolating back through the analysis magnet to the target vertex assuming its momentum to be elastic. Otherwise, P_5 was not used.

Using the predicted momenta and the measured scattering angles for the pion and proton, the projected transverse momenta, defined as:

$$p^{\pi}_{x(y)} = p'_{\pi} \sin\theta^{\pi}_{x(y)} \qquad p^{pr}_{x(y)} = p'_{pr} \sin\theta^{pr}_{x(y)}$$

were calculated. These quantities were used to determine the transverse momentum imbalance $\Delta p_{x(y)} = p^{\pi}_{x(y)} - p^{pr}_{x(y)}$ for the event (assuming it was elastic).

The program then calculated the proton trajectory beyond the analysis magnet, using the reconstructed proton track from the target and the predicted elastic momentum, and predicted the horizontal coordinate of the proton track in the P_6 proportional chamber. The calculated proton trajectory was required to intersect the hodoscope elements in F_α and F_β which were involved in the trigger. The distance between the calculated position in P_6, and the closest recorded hit, Δx_{p6}, was calculated.

b. Event Selection

After the events were reconstructed, histograms were made of the number of events versus the variables x_π, Δp_x, Δp_y and Δx_{p6}. These plots all showed the same characteristic feature events superimposed on a rather smooth background of inelastic events. A typical example is the histogram of x_π, the deviation of the true pion momentum from the expected elastic momentum, shown in fig. 6. The inelastic background is mostly to one side of the peak, as expected since the momentum of an inelastically scattered pion is always less than that of an elastically scattered pion produced at the same angle. The width of the peak directly reflects the momentum resolution of the backward spectrometer.

The final selection of elastic events was made by choosing those events which fell within a prescribed interval about the elastic peak of each of the 4 variables. The limits of this interval for a given variable were determined by observing the position and width of the elastic peak. The elastic cut thus defined was simply a cutoff value for the variable beyond which events were not considered to be elastic. To determine the optimum elastic cuts, several sets of histograms of the variables were generated.

In the first set, no cuts or very loose cuts were used. From these histograms, examples of which are given in the unshaded plots of figs 6-9, only an approximate determination of the elastic cuts could be made because the precise shape of the elastic peak was obscured by a large amount of inelastic background. Using these approximate cuts, another set of histograms was generated which contained a much lower proportion of background, allowing a more accurate determination of the shape of the elastic peak. A new set of cuts was then defined and another set of histograms generated. This iterative process was repeated until the final set of elastic cuts, wide enough to include all true elastic events yet sufficiently narrow to exclude the most inelastic background, was chosen.

The events accepted by the elastic cuts were used to generate a final histogram of the number of events versus the four-momentum transfer squared, u; the value of u for each event being calculated from the scattering angle of the backward pion. Events in this histogram consisted of the true elastic scatters and a small background of inelastic events topologically similar enough to elastic events to be accepted by the elastic cuts.

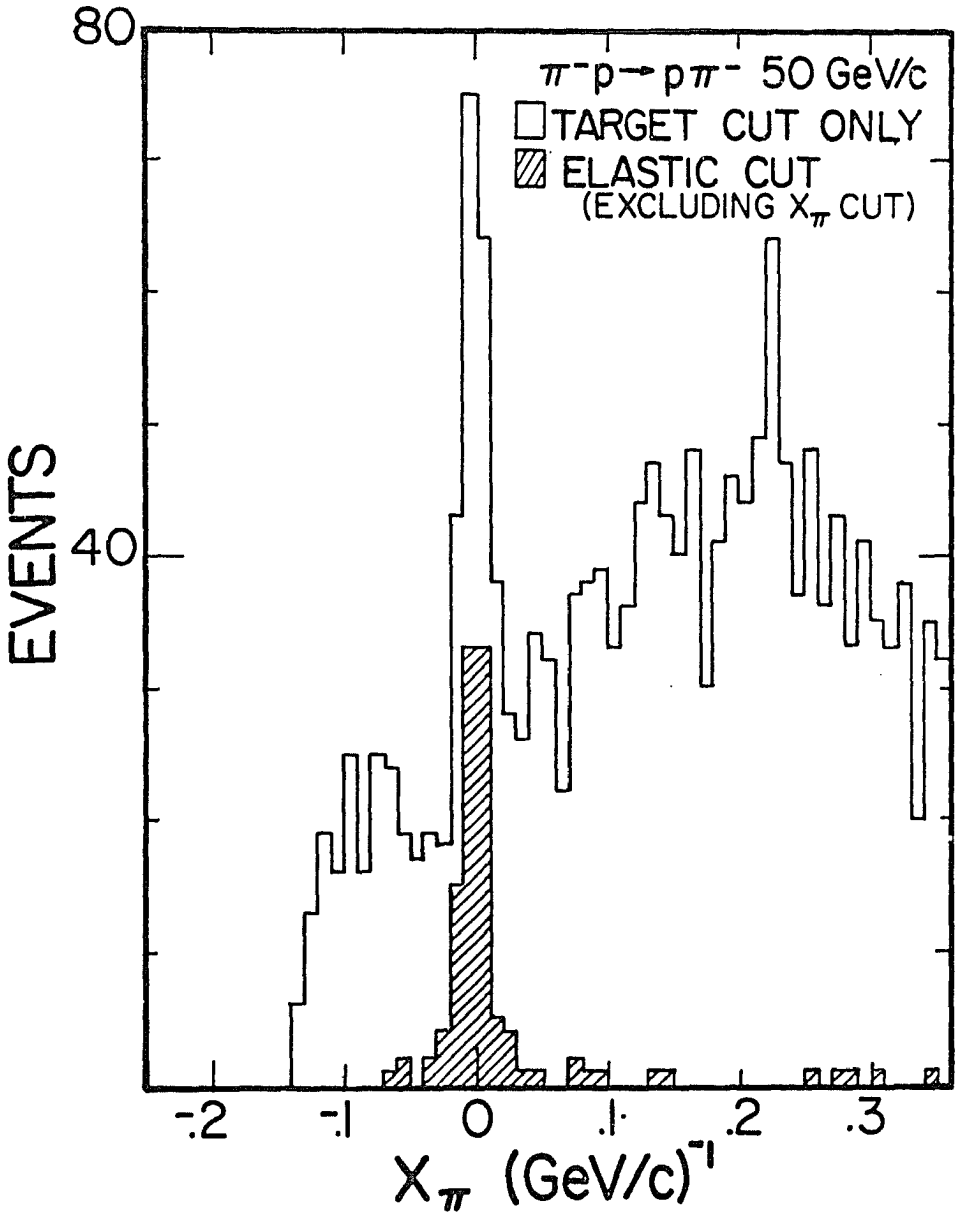

Figure 6. x_π Distribution.

Number of events vs. the variable x_π defined in the text.

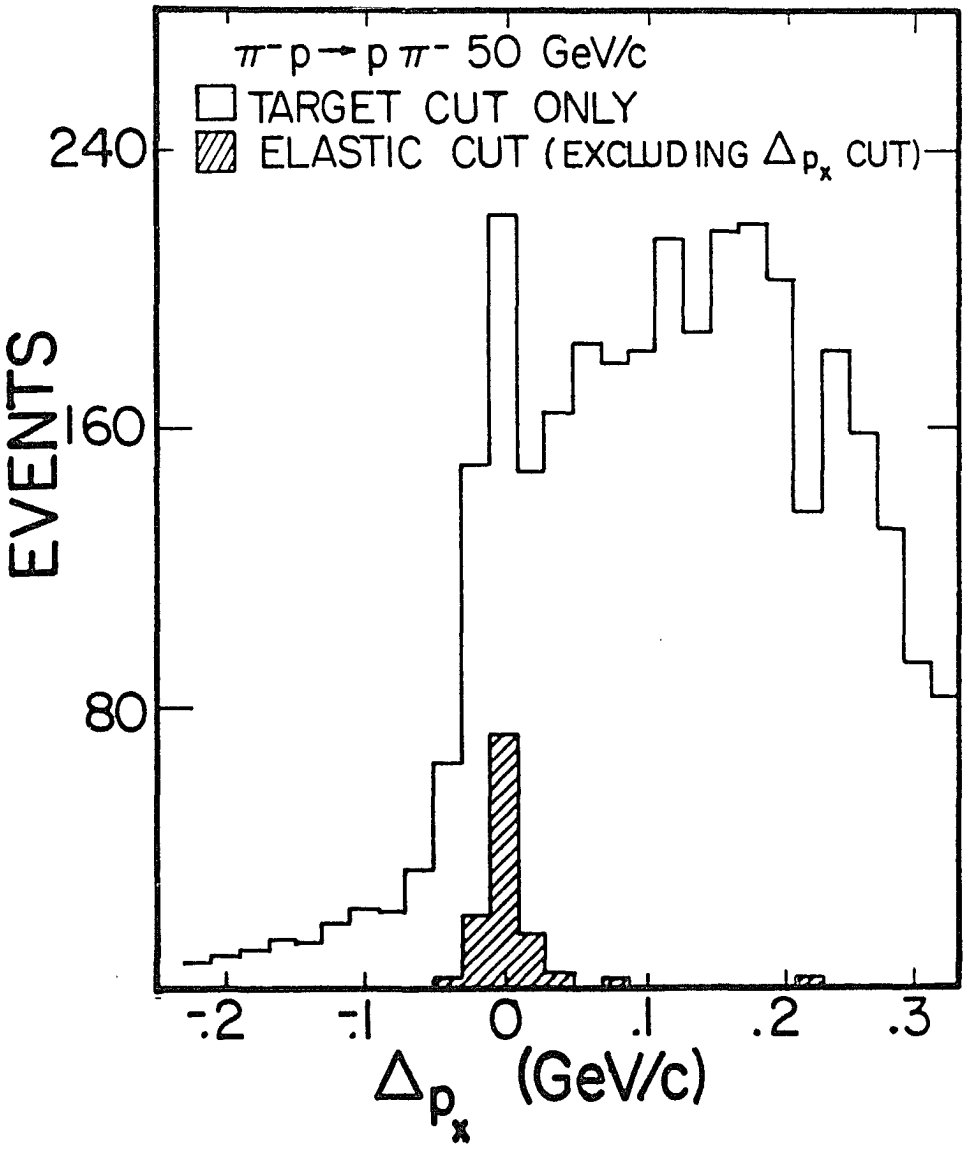

Figure 7. Δp_x Distribution.

Number of events vs. the projected (x) transverse momentum imbalance.

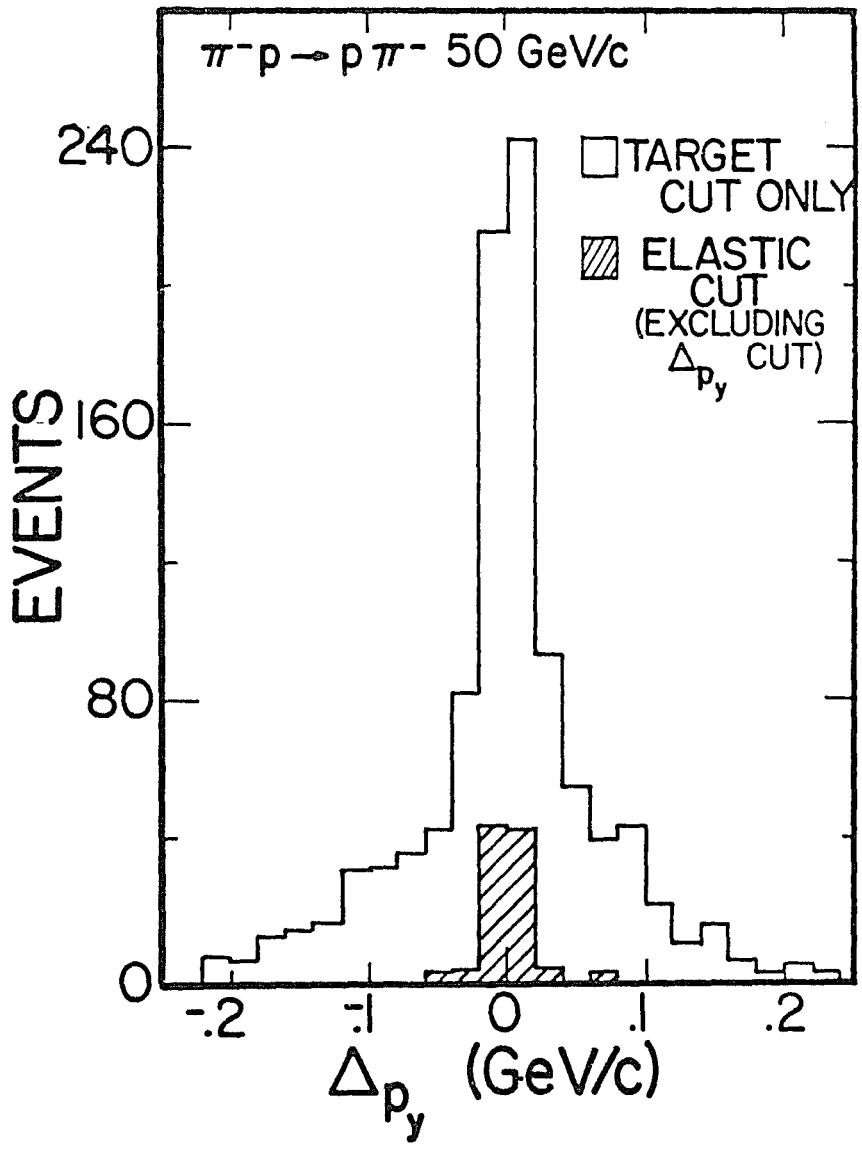

Figure 8. Δp_y Distribution.

Number of events vs. the projected (y) transverse momentum imbalance.

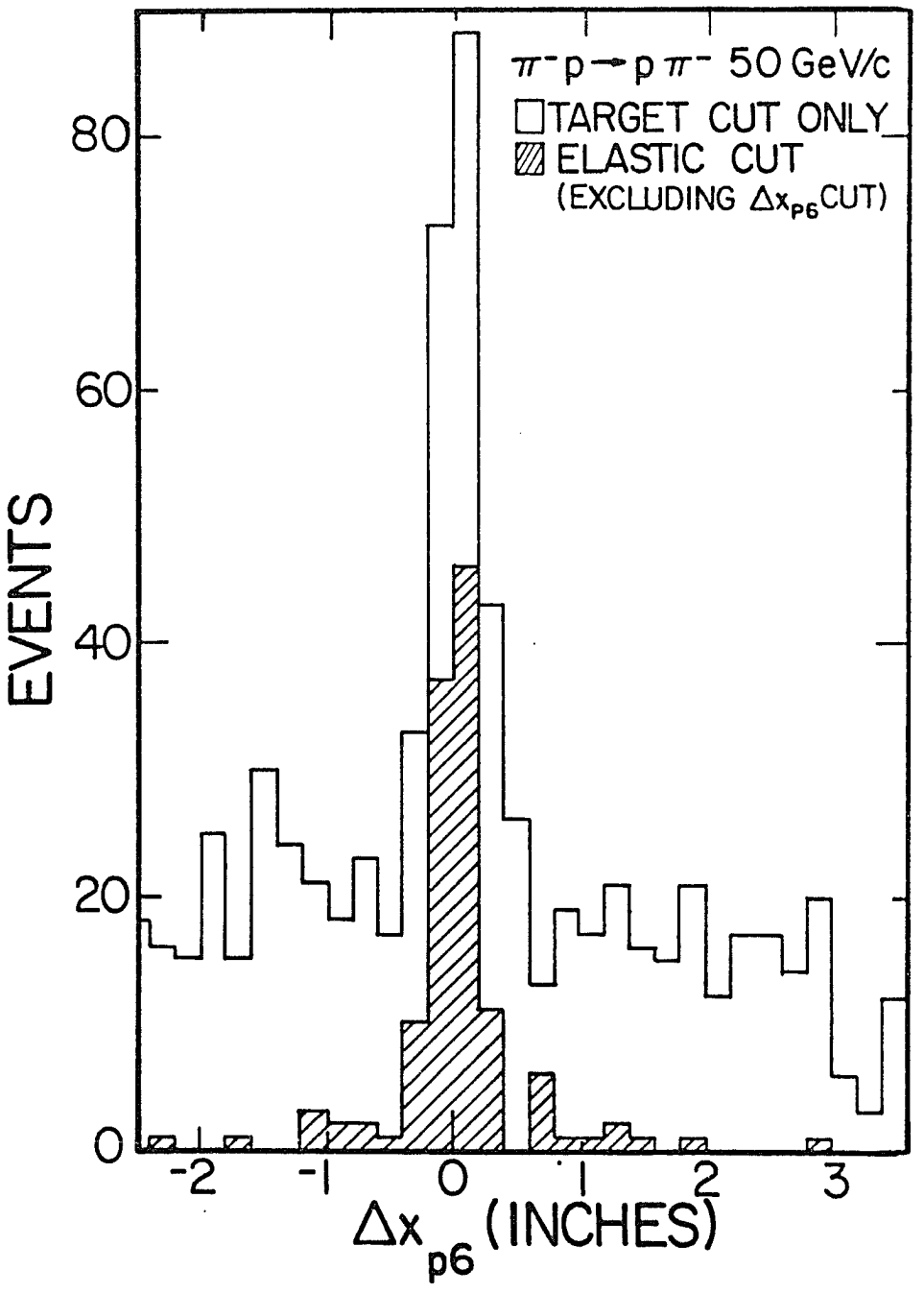

Figure 9. Δx_{p6} Distribution.

Number of events vs. the distance between the predicted position and the closest hit in chamber P_6.

c. Inelastic Background

Inelastic background in the final data sample was calculated using the distribution of events in the variable x_π. From a histogram similar to the shaded curve of fig. 6, the distribution of events surviving the elastic cuts on all the variables except x_π, the background outside the elastic peak was found to be approximately flat for positive x_π, and to eventually fall to zero for negative x_π. To determine the amount of background beneath the elastic peak, the assumption was made that it varied linearly from its level on one side of the elastic peak to its level on the other. A ± 50% systematic error was included in this determination to allow for uncertainty. The distribution of inelastic events in u was then determined by histograming the u values of events which satisfied the elastic cuts on all variables except x_π. For the latter, two cuts, each with a width equal to 1/2 that of the elastic cut, were placed on either side of the elastic peak to accept those inelastic events nearest, but outside, the peak. Assuming the inelastic events beneath the elastic peak had a similar distribution in u, a subtraction of the background could then be made. Since the statistics in this histogram were generally poor, fluctuations of the background level in u were smoothed out using a simple fit.

For the π^- data, the background subtraction was always less than 10% at 30, 50 and 70 GeV/c, but increased to $\sim$ 25% at 90 GeV/c for $-u \gtrsim 0.25$. For π^+, at 30 and 50 GeV/c and near $u = 0$ for 70 GeV/c, the subtraction again never exceeded 10%. However, at 70 GeV/c, in the region of the dip and beyond ($-u \geq .15$) the background became equal to the signal. Hence in this region, only upper limits are quoted for the cross section.

As was stated, this method of calculating the background assumed the number of inelastic events varied smoothly from the inelastic region through the elastic peak, and could be described by a linear form beneath the peak. In an effort to verify this assumption, a histogram was made of the distribution of events in x_π using the elastic cuts on Δp_x and Δp_y but with the cut on Δx_{p6} centered on the inelastic side of the elastic peak of that variable so as not to accept any elastically scattered protons. This histrogram, therefore, contained only inelastic events from which an attempt could be made to determine the shape of the background in the elastic peak region. Unfortunately, the statistics were poor and an exact determination was not possible. However, there was no significant change in the distribution of events going from the inelastic to the elastic region of x_π. Since the background subtraction was typically less than 10% of the total elastic signal, it

was concluded that within the elastic region the shape (for this purpose) was adequately described by a linear form.

The backward two-body inelastic processes, $\pi p \rightarrow \Delta\pi$ and $\pi p \rightarrow p\rho$, could also result in a peak in the x_π distribution which would overlap with the elastic peak. Since such processes might not be properly subtracted by the above mentioned procedure, a Monte-Carlo study was performed to determine what fraction of the events from each process would be accepted by the analysis program as elastic. The results showed this fraction to be less than 1.0% for either process for incident momenta between 30 and 90 GeV/c. Since the cross sections for these processes have been measured to be less than the backward elastic cross section, at least at lower energies [25-27], their contribution to the results was concluded to be negligible.

d. Corrections

The measured cross sections were corrected for muons and electrons in the pion beam (1.5-12.7%); more than one beam particle in an rf bucket (2%); absorption in the hydrogen target, air, Cerenkov counter mirrors, MWPC's, and counters ($\sim$ 30-34%); and accidental vetos of elastic events by delta rays produced in the target (4.9%).

The geometrical acceptance of the apparatus at each incident momentum was determined by a Monte Carlo program. Elastic events were generated in the hydrogen target with a random distribution in azimuthal angle, and the scattered particles propagated through the spectrometer arms. The measured incident beam parameters (momentum spread, divergence and spot size) were properly accounted for as were the effects of multiple coulomb scattering. The probability of detecting an event was calculated as a function of the four momentum transfer squared, u. The parent distribution in u from which Monte-Carlo events were generated was chosen to approximate the experimentally measured distributions, so that the results statistically would better represent the experimental situation. The acceptance curve for scattering at 30 GeV/c is shown in fig. 10. The curves for the other incident momenta are quite similar. Because the overall acceptance was essentially determined by the fixed vertical acceptance of the S-hodoscope counter, the acceptance curve exhibits an approximate $1./\sin(\theta)$ dependence, as is expected for this type of geometrical constraint.

Proportional chamber efficiencies, measured during special calibration runs at various times during the data taking, varied betweeen 85-98% depending on the chamber. Chamber response as a function of time was very stable.

The efficiency of the analysis program in identifying elastic events as a function of u was measured using Monte-Carlo generated events. Included in the event generating procedure were the effects of MWPC spacial resolution, MWPC efficiency, multiple Coulomb scattering, incident beam phase space and scattered pion decay. The generated MWPC and hodoscope data were overlaid with real data taken at random times during the beam spill which added a suitable background. The resulting events were then processed by the analysis program. Including the effects mentioned above, between 78-86% of the elastic events were idenfitied as such. Most of the events that were not identified as elastic lacked sufficient MWPC data due to the measured chamber efficiencies included in the program. Assuming the chambers were 100% efficient, the program was able to identify > 98% of the Monte-Carlo events as being elastic.

Radiative corrections, as pointed out by Sogard [28], may be substantial and were calculated using the procedure outlined in refs 26-31. For π^+p scattering, the correction was negligible; for π^-p the correction changed the overall normalization of the differential cross sections by a factor 1.14-1.18 depending on momentum, independent of scattering angle.

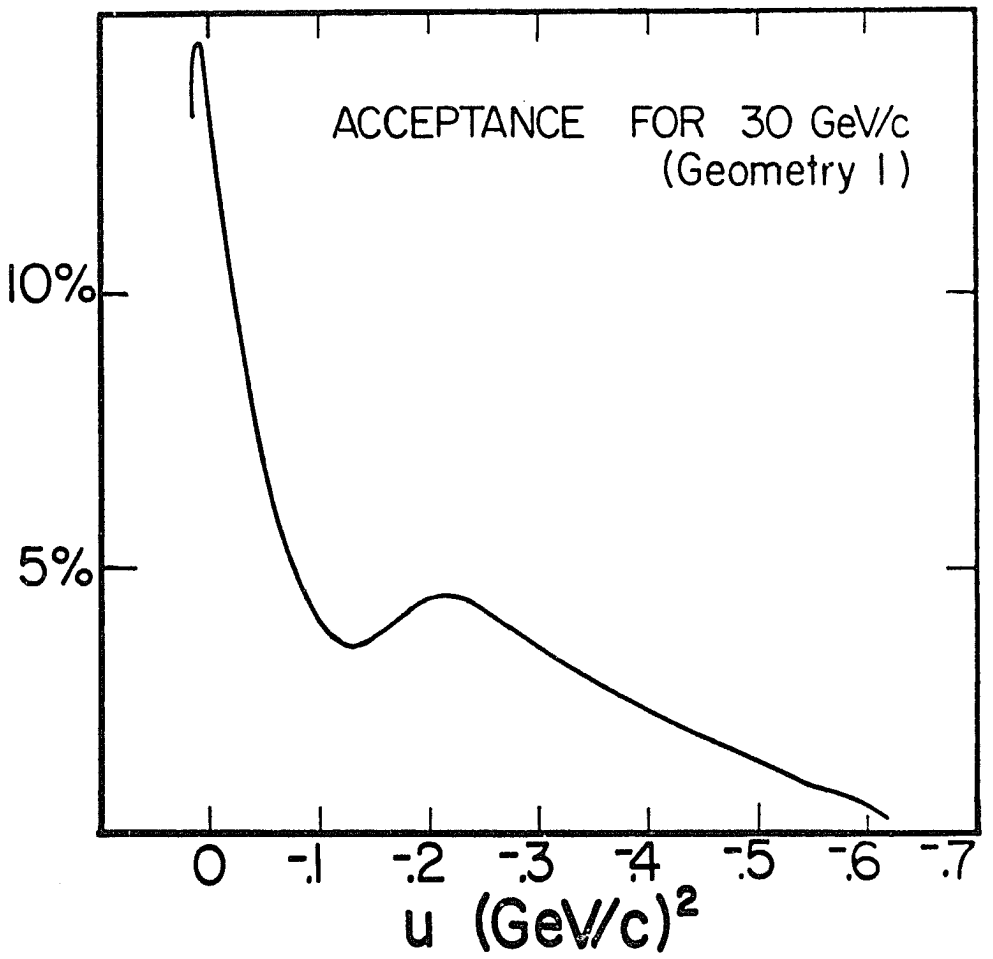

Figure 10. Experimental Acceptance.

For incident momentum of 30 GeV/c.

Several runs were taken with the target empty to determine the contribution from events not originating in the liquid hydrogen. The results of the analysis of these runs indicated such a contribution was negligible.

CHAPTER 4

RESULTS

The results are presented in tabular form in Tables 2 and 3 and graphically in figs. 11 and 12 (together with some earlier results). The errors quoted are statistical and represent one standard deviation. For those bins in which no signal above background was found, the cross sections are given as upper limits and represent a 90% confidence level. Because of uncertainties in the previously discussed corrections, the uncertainty in the overall normalization of the cross sections is estimated to be ± 15%.

a. General Features

1) The u distributions of the cross sections $d\sigma/du$ for both π^+ and π^- measured above 30 GeV/c are similar to those previously obtained below 18 GeV/c. In figs. 11 and 12, the results may be compared with the π^+ results of Baker et al., at 7 GeV/c and the π^- results of Owen et al. at 6 GeV/c. For π^+ scattering the steep backward peak and the dip at $-u = 0.15$ $(\text{GeV/c})^2$ as well as the broad second maximum between $-u = .25$ and $.45$ are all present, at least up to 50 GeV/c. The data at 70 GeV/c are also consistent with these features.

Figure 11. Backward π^+p Elastic Scattering Differential Cross-Sections.

Upper limits are 90% confidence. Solid lines are fits of the form e^{Bu} for $-u < .1$ to the data of this experiment and those of Babaev and co-workers (ref. 20). Results of Baker et al. (ref. 5) are represented by a dashed curve. Remaining dashed lines are to guide the eye. Note the data are scaled by the given factors to separate clearly the data points at different momenta.

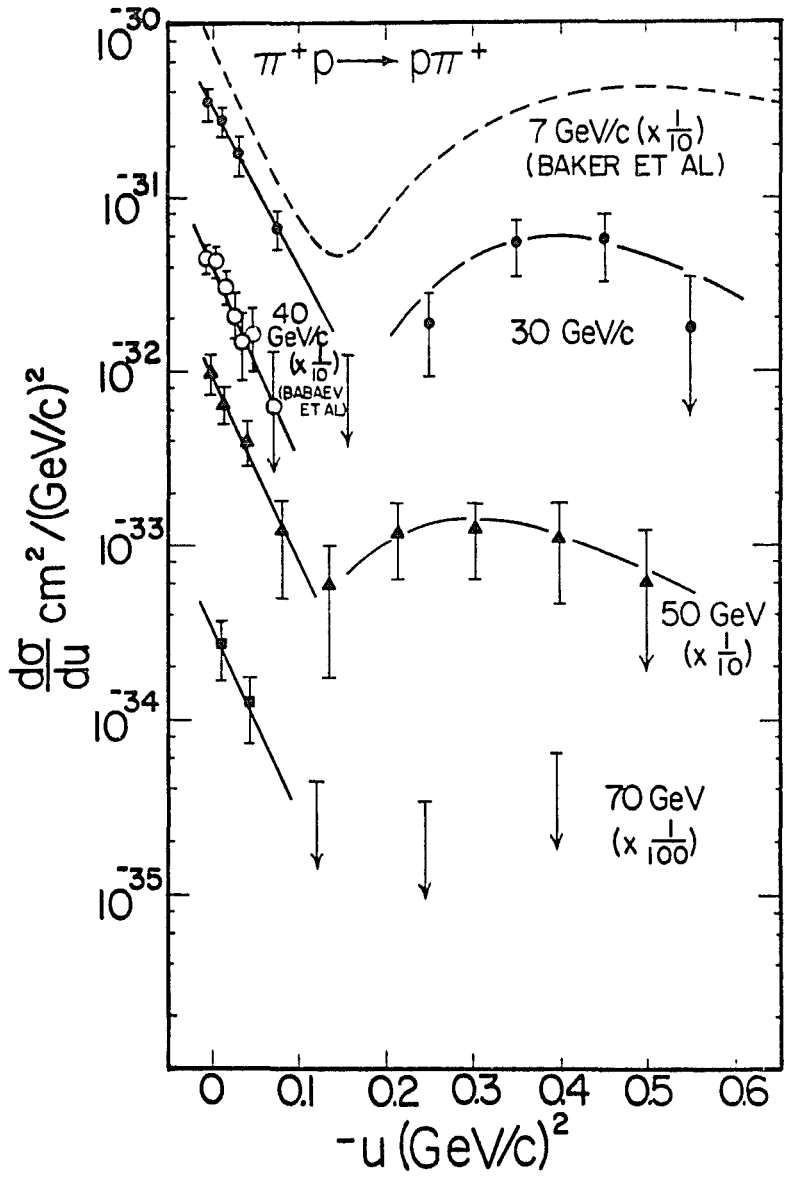

Figure 11. Backward π^+p Elastic Scattering Differential Cross-Sections.

Figure 12. Backward $\pi^- p$ Elastic Scattering Differential Cross-Sections.

Upper limits are 90% confidence. Solid lines are fits of the form e^{Bu} for $-u < .5$ to the data of this experiment and those of Babaev and co-workers (ref. 21). Results of Owen et al. (ref. 4) are represented by a dashed curve. Note the data are scaled by the given factors to separate clearly the data points at different momenta.

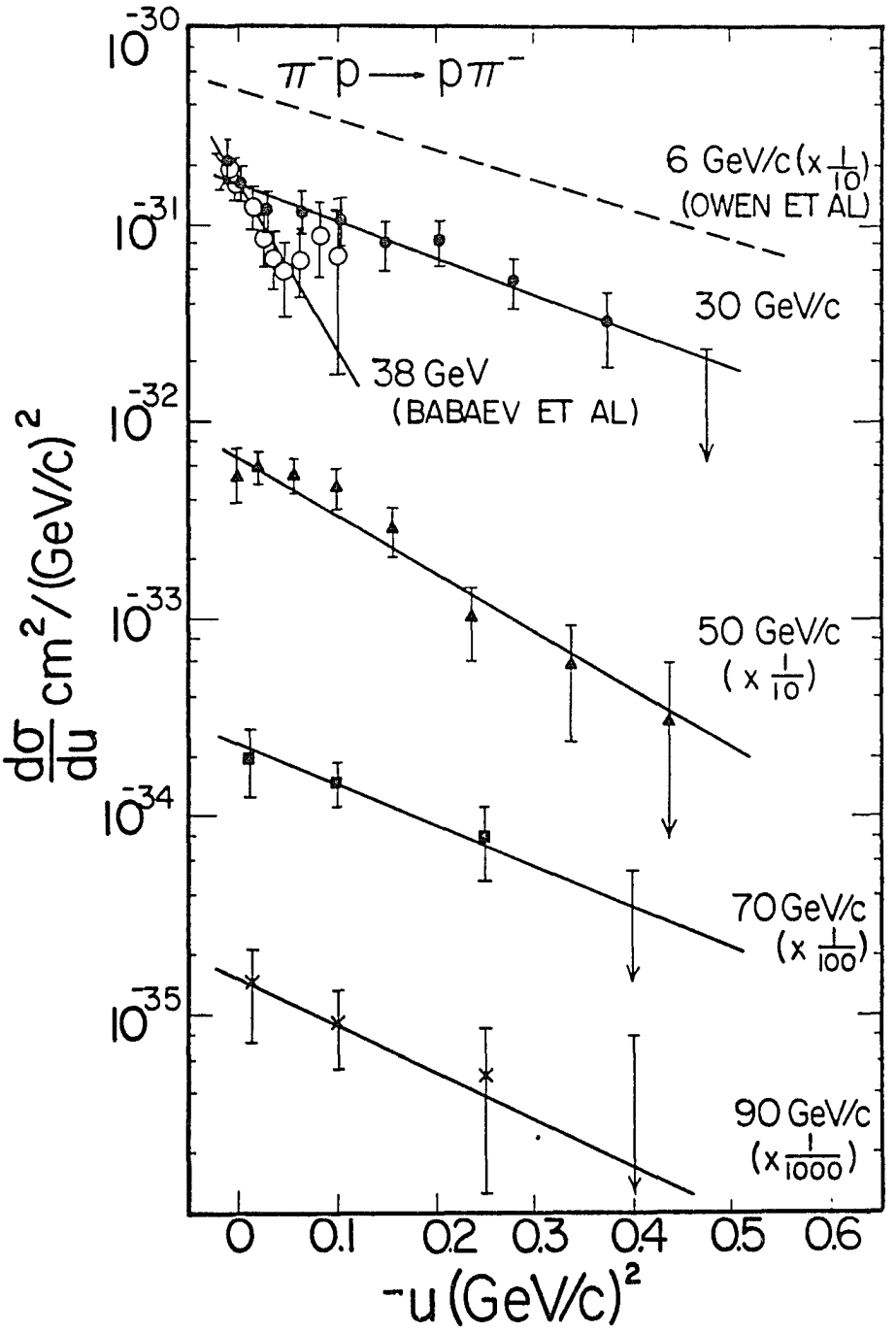

Figure 12. Backward $\pi^- p$ Elastic Scattering Differential Cross-Sections.

2) In the region of the backward peak, the cross section has an approximately exponential dependence on u. The data in the region $-u < 0.1$ $(GeV/c)^2$ for positive pion scattering and $-u < -0.5$ for negative pion scattering were fitted using the relation $d\sigma/du = Ae^{Bu}$. The fitted values for A and B are given in Table 4. The values of B range from 21 to 26 $(GeV/c)^{-2}$ for positive pion scattering and from 4 to 7 $(GeV/c)^{-2}$ for negative pion scattering. These are compared with the values of B obtained at lower energies in fig. 13. For both polarities, they are consistent with a slow increase in B for incident momenta between 5 GeV/c and 90 GeV/c.

3) The cross section $d\sigma/du$ at $u = 0$ for π^+p is greater than for π^-p at all measured momenta. The ratio of π^+p/π^-p varies from 1.9 at 30 GeV/c to 1.5 at 70 GeV/c.

The cross section $d\sigma/du$, at $u = 0$, for both positive and negative pions, decreases with increasing momentum. The available data above 5 GeV/c including our own have been fitted to the form:

$$\frac{d\sigma(p,u = 0)}{du} = Ap^{-n} .$$

It was assumed, as indicated by the data, that the above parametrization was reasonable. For the fits the quoted statistical and systematic errors were added in quadrature for each experiment. For π^+, the data from Babaev et al. at 23 and 38 GeV/c were not included in the fits (for

Figure 13. Slope of Backward Elastic Peak as a Function of Laboratory Momentum.

Results of fits of the backward slope parameter B. The data shown are for this experiment and from refs. 2-7, 9, 20-21. The solid lines are fits to the form:

$$B = 2 \cdot \ln p_{lab} + \text{constant}$$

for each pion polarity.

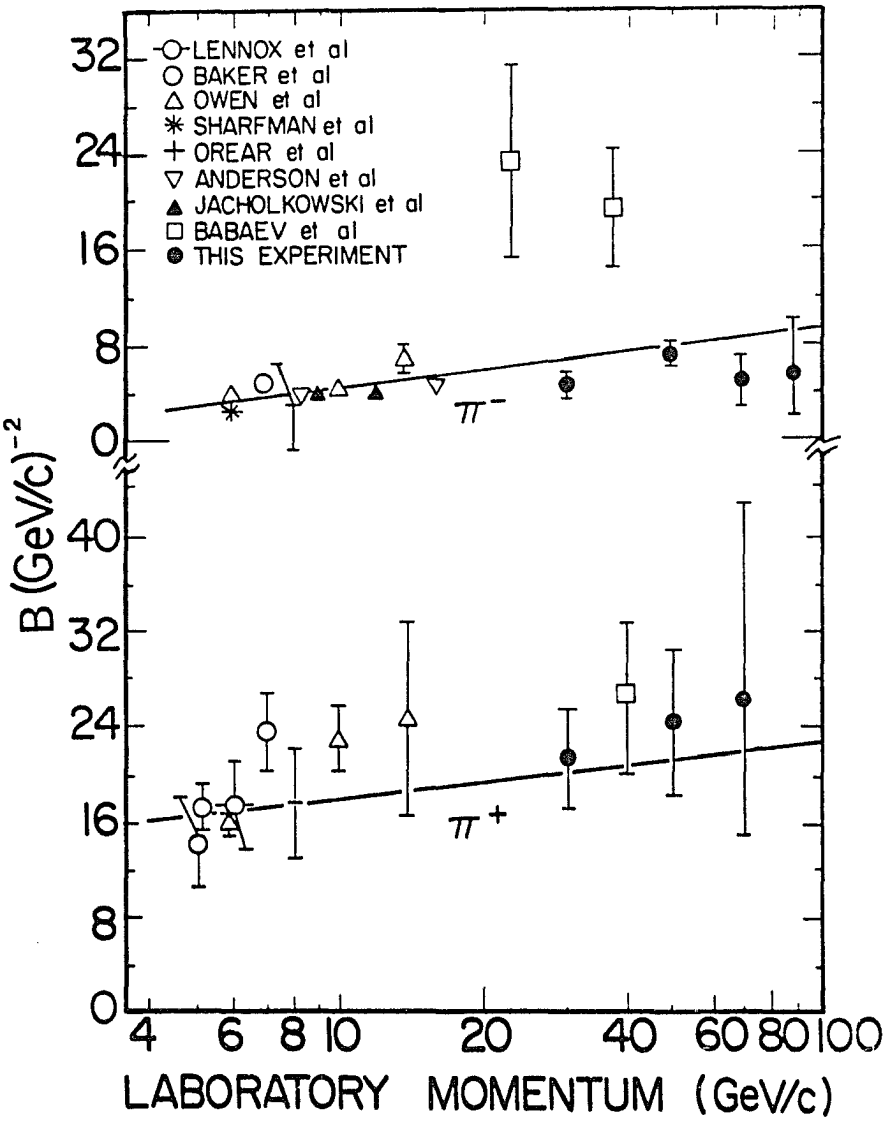

Figure 13. Slope of Backward Elastic Peak as a Function of Laboratory Momentum.

Figure 14. Momentum Dependence of Elastic Differential Cross-Section at u = 0.

(a,b). Results for $d\sigma/du$ at u = 0. The data shown are from this experiment and from refs. 2-5, 7, 9, 20-21. Curves are from fits to the form

$$(d\sigma/du)\big|_{u=0} = Ap^n$$

with $n^-=-2.08$ and $n^+=-2.31$ in (a) and (b) respectively, as described in the text.

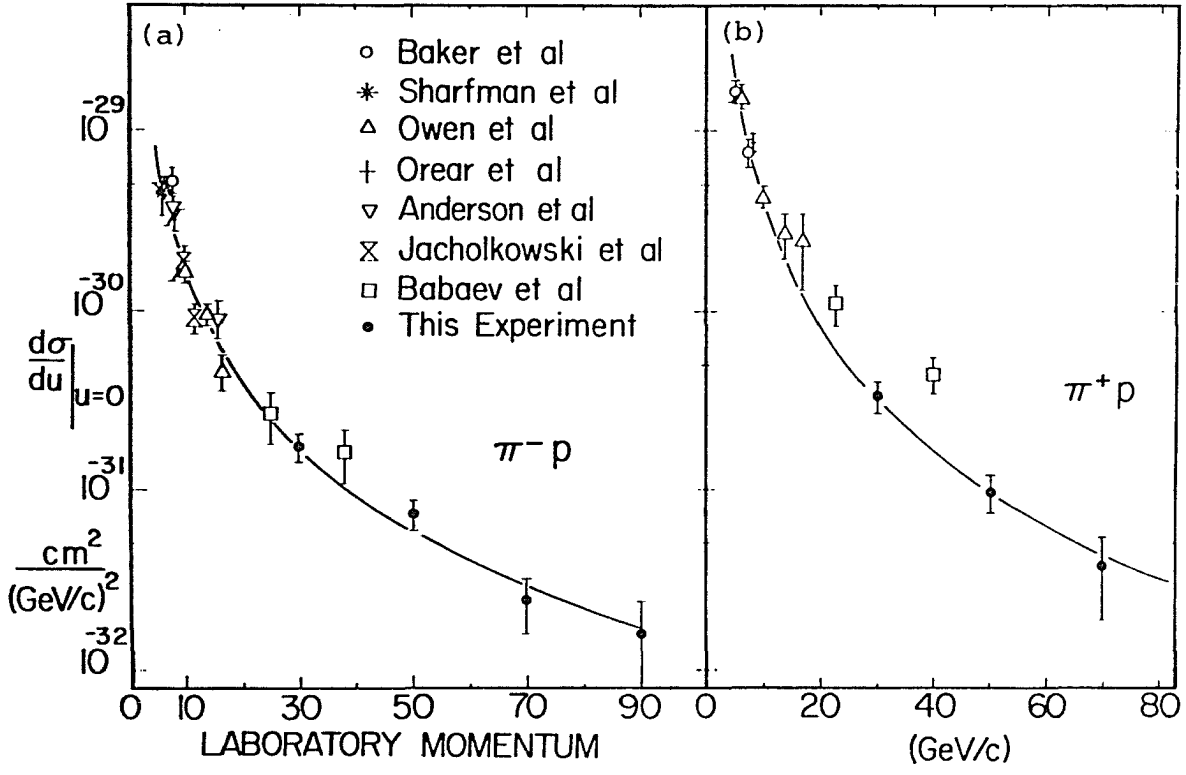

Figure 14. Momentum Dependence of Elastic Differential Cross-Section at u = 0.

reasons explained below). The results are shown in figs. 14(a,b). We obtain the values $n^+=2.31 \pm 0.07$ and $n^-=2.08 \pm 0.06$ with χ-squared probabilities of 26% and 21% respectively. Local fits to the data of this experiment only, assuming the above parametrization have also been performed and yield the values $n^+=2.51 \pm 0.21$ and $n^- = -2.11 \pm 0.21$. Within errors, the two sets of results are consistent.

5) The data do not confirm the large values of $d\sigma/du$ at u=0 for π^+p scattering, nor the very sharp increase in the π^-p cross section as 180^0 is approached, observed in the data of Babaev and co-workers. As shown in fig. 14(b), the previous 40 GeV/c π^+p result is approximately 2.5 times larger than that expected from a smooth interpolation between the measurements of this experiment at 30 and 50 GeV/c. The angular distributions however are quite similar (see fig. 11). For π^- scattering, the two experiments observe substantially different angular distribution as shown in fig. 13 where the 38 GeV/c Babaev results have been included for comparison. Exponential fits to the Serpukhov data yield values for the parameter B between 19 and 23 in comparison to the values of B between 4 and 7 for this experiment. It should be pointed out that their data covered a much narrower u range than ours, hence their fits were limited to the region very close to u=0. The possibility that a real physics effects near

u=0 leads to a sharp peak in the π^- distribution cannot entirely be ruled out, however our data, particularly at 50 GeV/c do not support this hypothesis.

b. Discussion

As was mentioned in the Introduction, many of the features of both π^+p and π^-p backward elastic scattering above the resonance region and below 18 GeV/c can be explained by a simple Reggeized baryon exchange model. The same is found to be true for the data obtained by this experiment between 30 and 90 GeV/c. In the model, the dip in the π^+p differential cross section at $-u = 0.15$ occurs because the amplitude of the nucleon trajectory (assumed to dominate this process) vanishes at this u value. Since in π^-p scattering the exchange of the nucleon trajectory cannot occur, a dip at this u value is neither expected nor seen.

The model also predicts the width of the backward peaks to slowly decrease with increasing momentum. Specifically, given that the backward peaks at all energies may be parameterized by the form Ae^{Bu}, the parameter B is expected to increase with increasing momentum as $B=2\ln(p_{lab})$ + constant. The data above 5 GeV/c including that of this experiment, as shown in fig. 13 are consistent with this form.

As was mentioned before, it is assumed in the simple Regge model that the π^+p backward cross section is dominated by the exchange of the N_α trajectory, at least at lower energies. In general, any baryon exchange model would allow for the exchange of the N_α, N_γ and Δ_δ trajectories in π^+p scattering and the exchange of only the Δ_δ trajectory in π^-p scattering. The assumption that the N_α trajectory dominates π^+p scattering is based on the following reasoning. It is known that for π^-p scattering, in which only the Δ_δ trajectory can be exchanged, the backward cross sections are less than for π^+p scattering, at least up to the highest energies measured so far. Since the Δ_δ contribution to the π^+ cross section is 1/9 its contribution to the π^- cross section (1/9 being the necessary Clebsch-Gordon coefficient) its contribution to the overall π^+ cross section is concluded to be small. The argument that the N_γ contribution is smaller than the N_α is based on the observation that in the region near $-u=0.15$ where the N_α amplitude vanishes, the π^+p cross section decreases by more than an order of magnitude compared with its value at $u=0$. Since the N_γ amplitude is not predicted to vanish near $-u=0.15$, the level of the cross section in the dip should reflect an upper limit on the N_γ contribution. Also, since the N_γ trajectory lies below that of the N_α (as determined from the Chew-Frautschi

nucleon and isobar mass plots [i.e $\alpha_{N\gamma}(u) < \alpha_{N\alpha}(u)$]) and since the cross section $d\sigma/du$ for the exchange of a single trajectory falls as $s^{2\alpha(u)-2}$, the influence of N_γ exchange should decrease with increasing energy. It should be noted that the above arguments assume the Regge trajectories are linear, and therefore that the zero of the N_γ scattering amplitude, which occurs when $\alpha_{N\gamma}(u)=-3/2$ does not occur at the value of u corresponding to the π^+p dip.

The Regge model prediction that the cross section $d\sigma/du$ decreases for any value of u with increasing momentum as $s^{2\alpha(u)-2}$ where s is the CMS energy squared and $\alpha(u)$ is the trajectory of the exchange Reggeon, can be used to derive an effective Regge trajectory which describes the scattering process. This effective trajectory can be compared with the expected forms of the Δ_δ and the N_α trajectories assumed to dominate π^- and π^+ scattering respectively as a check of the validity of the Regge model. The available π^- and π^+ backward elastic data above 5 GeV/c including that of this experiment and also the data of this experiment alone have been fitted using this parameterization for several values of u in the range $0 < -u < 0.5$. The chi-squared probabilities of the fits, which vary from 50% to 5% and 70% to 10% as -u increases from 0 to 0.5 for π^+ and π^- scattering respectively, are in indication that this parameterization

describes the data reasonably well. In the fitting procedure, a 15% systematic error was added to the quoted statistical error of each experiment to allow for uncertainty in the absolute normalization of the different experiments. The results of the fits, expressed in terms of $\alpha(u)$ are shown in figs 15 and 16 for π^- and π^+ scattering respectively.

For π^-p scattering, a linear least squares fit to the effective trajectory gives $\alpha(u) = -0.06 \pm 0.05 + (0.50 \pm 0.26)u$ for the 5-90 GeV/c data and $\alpha(u) = -0.11 \pm 0.14 + (0.67 \pm 1.04)u$ for the 30-90 GeV/c fits to the data of this experiment only. These results are not inconsistent with the form of the Δ_δ trajectory, $\alpha_{\Delta_\delta}(u) = 0.0 + 0.9u$, obtained from Regge fits at lower energies. The $u = 0$ intercept of the effective trajectory near $\alpha(u) = 0$ gives the momentum dependence of the cross section $d\sigma/du$ at $u = 0$ of $p_{lab}^{-2.0}$ predicted by the model. Our results for $d\sigma/du$ as a function of u at 50 GeV compare well with the prediction of the simple Regge model of Berger and Fox [16] as shown in fig. 17, except perhaps near $u \approx 0$ where the model predicts a somewhat lower cross section.

For π^+p scattering, we find the linear fit to the effective trajectory of the 5-70 GeV/c data, $\alpha(u) = 0.15 \pm 0.06 + (2.24 \pm 0.25)u$, to be somewhat steeper in u than expected for the N_α trajectory, which from low energy Regge fits and Chew-Frautschi plots may be parameterized as $\alpha(u) = -0.39 + 1.0u$. However, the

effective trajectory derived from the data of this experiment only, $\alpha(u) = -0.37\pm0.11 + (0.58\pm0.50)u$, is found to be in better agreement. The higher $u = 0$ intercept of the effective trajectory from the 5-70 GeV/c data, $\alpha(u) = -0.15$, gives a momentum dependence for $d\sigma/du$ at $u = 0$ of $p_{lab}^{-2.31}$ as opposed to the $p_{lab}^{-2.7}$ dependence predicted by the model. As a result of this discrepancy, the prediction for the momentum at which the π^- cross section becomes larger than the π^+ is raised to $\sim$ 400 GeV/c. The distribution in u of $d\sigma/du$ observed in our data at 50 GeV/c agrees well with the prediction of the model in shape, and in magnitude throughout the entire u range of $0. < -u < 0.5$ when the prediction is normalized to the measured cross section at $u = 0$ as shown in fig. 17.

The above results encourage the interpretation of backward $\pi^{\pm}p$ elastic scattering between 30-90 GeV/c by a simple Reggeized baryon exchange model, as at lower energies. Future experiments, at still higher energies, could resolve some outstanding questions and provide crucial tests of the model. Specifically, does the π^-p backward cross section become larger than the π^+, and does the u distribution of the π^+p cross section similar to the π^-p, as would be expected if the exchange of the Δ_δ trajectory dominated both processes. The difficulty of such experiments however, in view of the low cross sections predicted, should not be underestimated.

Figure 15. Effective Regge Trajectory for $\pi^- p$ Backward Elastic Scattering.

Derived in the manner described in the text. Data used to determine the trajectory in (a) are from this experiment, and refs. 2-5. Data used to determine trajectory in (b) are from this experiment only. The solid line is a linear fit to the data. The dashed line is the Δ_δ trajectory mentioned in the text.

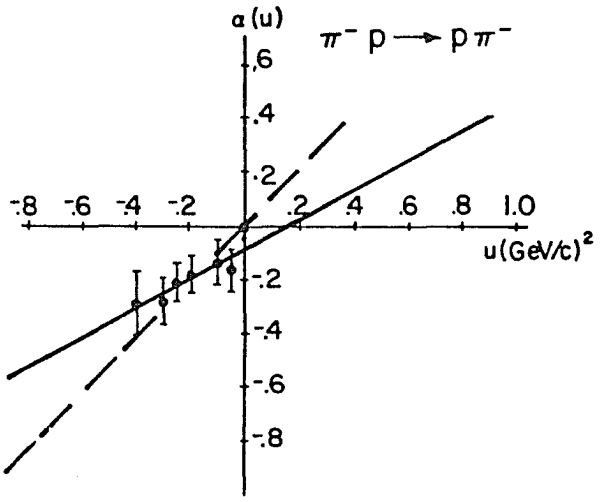

(a)

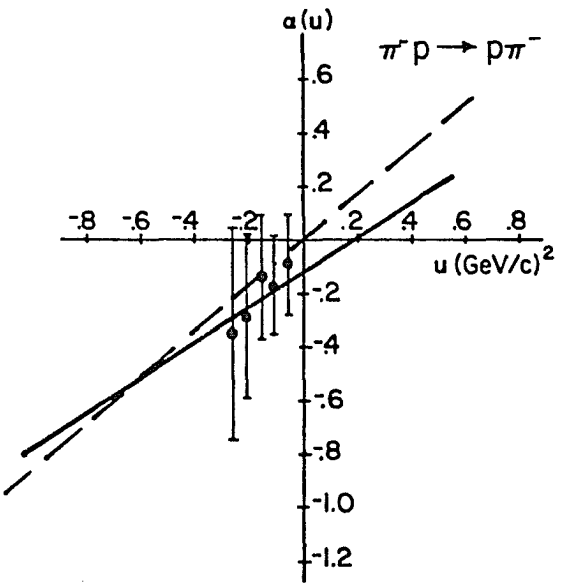

(b)

Figure 15. Effective Regge Trajectory for $\pi^- p$ Backward Elastic Scattering.

Figure 16. Effective Regge Trajectory for π^+p Backward Elastic Scattering.

Derived in the manner described in the text. Data used to determine trajectory in (a) are from this experiment, and refs. 2, 4-5. Data used to determine trajectory in (b) are from this experiment only. The solid line is a linear fit to the data. The dashed line is the N_α trajectory mentioned in the text.

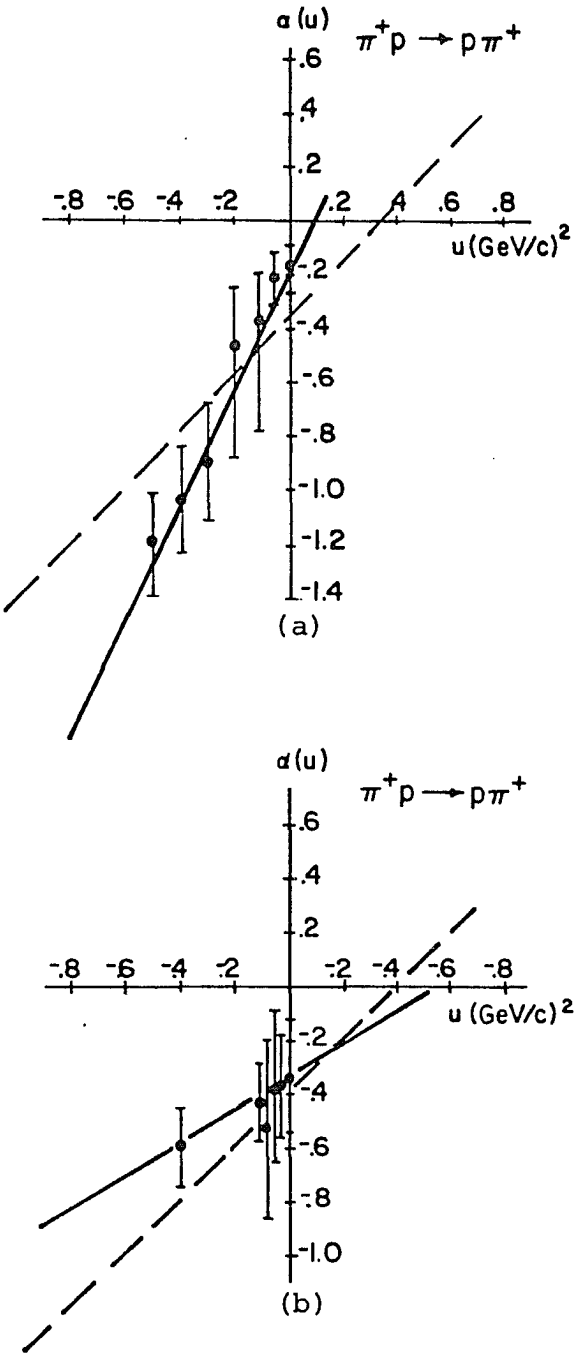

Figure 16. Effective Regge Trajectory for π^+p Backward Elastic Scattering.

Figure 17. Comparison of the Results at 50 GeV/c for $d\sigma/du$ for π^+ and π^- Backward Elastic Scattering with the Predictions of a Simple Regge Model.

Comparison of the results of this experiment to the predictions of the simple Regge model discussed in ref. 16. Solid lines are the predicted cross sections. Dashed line through the π^+ data is the predicted π^+ cross section normalized to the measured cross section at $u = 0$.

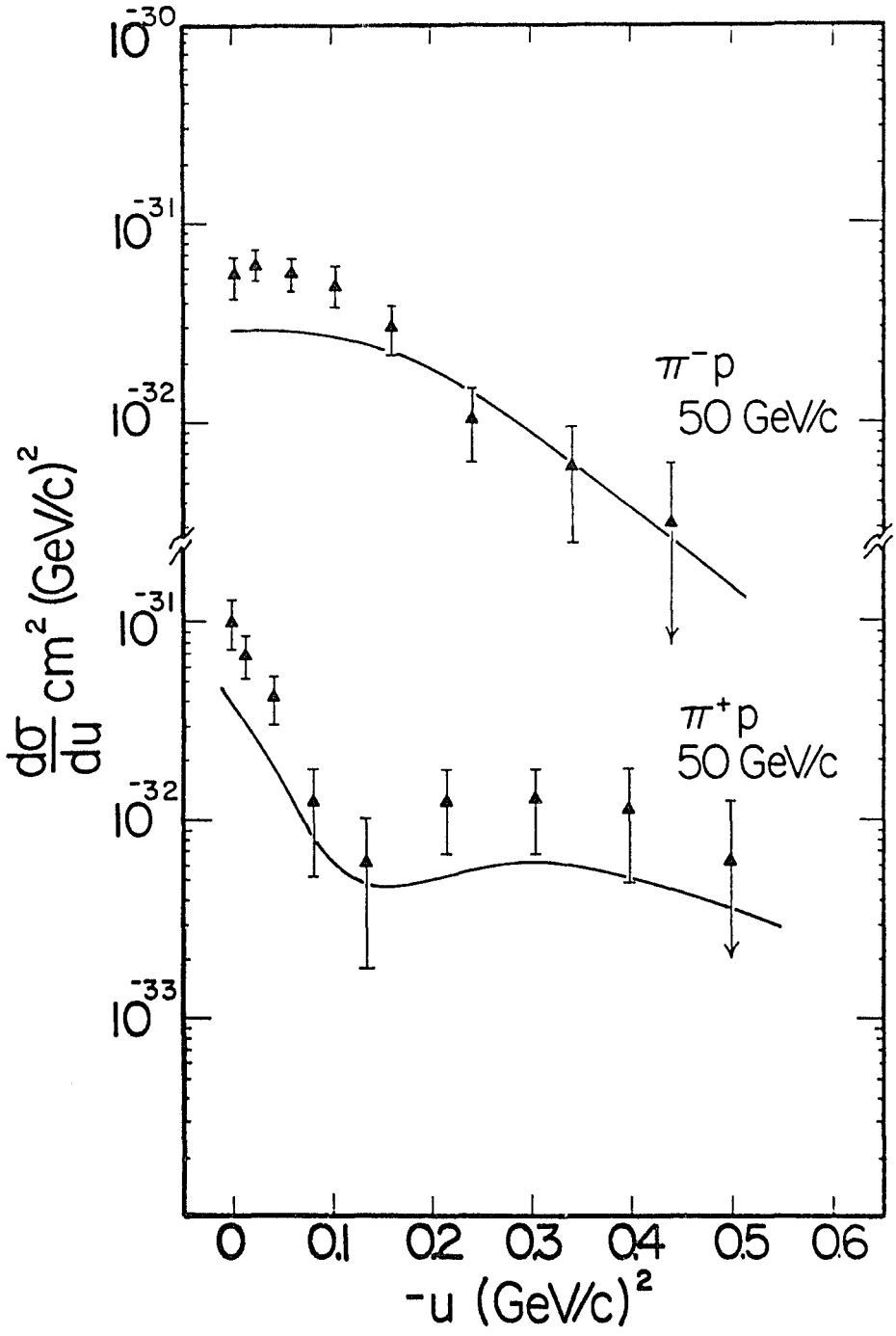

Figure 17. Comparison of the Results at 50 GeV/c for $d\sigma/du$ for π^+ and π^- Backward Elastic Scattering with the Predictions of a Simple Regge Model.

Table 2. π^+p Backward Elastic Differential Cross-Sections.

Incident momentum (GeV/c)	u $(GeV/c)^2$	Δu $(GeV/c)^2$	$\frac{d\sigma}{du}$ $\frac{nb}{(GeV/c)^2}$	Error $\frac{nb}{(GeV/c)^2}$
30.0	+0.003	0.011	351.1	62.6
	-0.011	0.018	270.4	51.1
	-0.030	0.020	176.9	43.5
	-0.075	0.070	66.4	17.1
	-0.115	0.090	<12.3	
	-0.250	0.100	18.6	9.3
	-0.350	0.100	54.1	19.1
	-0.450	0.100	56.5	23.1
	-0.550	0.100	17.4	17.4
50.0	0.000	0.008	96.9	25.9
	-0.014	0.020	65.2	15.8
	-0.042	0.036	40.4	11.2
	-0.080	0.040	11.8	6.8
	-0.135	0.070	5.8	4.1
	-0.215	0.090	11.8	5.3
	-0.305	0.090	12.1	5.6
	-0.400	0.100	10.9	6.3
	-0.500	0.100	6.0	6.0
70.0	-0.011	0.018	26.6	9.7
	-0.045	0.050	12.2	5.1
	-0.120	0.100	< 4.4	
	-0.245	0.150	< 3.3	
	-0.395	0.150	< 6.3	

Table 3. $\pi^- p$ Backward Elastic Differential Cross-Sections.

Incident momentum (GeV/c)	u $(GeV/c)^2$	Δu $(GeV/c)^2$	$\frac{d\sigma}{du}$ $\frac{nb}{(GeV/c)^2}$	Error $\frac{nb}{(GeV/c)^2}$
30.0	+0.004	0.008	225.2	53.1
	-0.010	0.020	172.5	33.2
	-0.035	0.030	125.4	27.4
	-0.070	0.040	124.2	29.3
	-0.110	0.040	111.2	30.9
	-0.155	0.050	85.0	24.5
	-0.210	0.060	86.9	22.4
	-0.285	0.090	53.6	15.5
	-0.380	0.100	33.2	13.6
	-0.480	0.100	<23.4	
50.0	-0.004	0.013	55.8	13.6
	-0.025	0.030	62.7	11.4
	-0.060	0.040	60.0	11.2
	-0.105	0.050	49.9	11.8
	-0.160	0.060	30.2	8.6
	-0.240	0.100	10.7	4.3
	-0.340	0.100	6.0	3.5
	-0.440	0.100	3.1	3.1
70.0	-0.013	0.024	20.8	7.4
	-0.100	0.150	15.8	4.1
	-0.250	0.150	8.1	3.3
	-0.400	0.150	<5.5	
90.0	-0.014	0.023	15.2	7.6
	-0.100	0.150	9.4	3.9
	-0.250	0.150	5.1	3.8
	-0.400	0.150	< 7.8	

Table 4. Results of Exponential Fits of the Backward Peaks.

Incident Momentum (GeV/c)	A $\frac{nb}{(GeV/c)^2}$	B $(GeV/c)^{-2}$
+30.0	333.8 ± 43.4	21.4 ± 3.8
+50.0	96.7 ± 18.9	24.3 ± 6.0
+70.0	36.8 ± 15.7	26.3 ± 13.1
-30.0	175.0 ± 20.0	4.37 ± 0.78
-50.0	73.2 ± 8.8	6.89 ± 0.92
-70.0	24.1 ± 6.6	4.71 ± 1.97
-90.0	16.1 ± 7.5	5.07 ± 4.01

APPENDIX A

FAST LOGIC

The fast logic used in this experiment may be divided into four logical subgroups: (1) the Beam Logic, (2) the Slow or Backward Arm Logic, (3) the Fast or Forward Arm Logic and (4) the Gating Logic. Detailed diagrams of each group are given in figs. 18-21 and each is described below. The entire fast logic system was composed of logic units manufactured by LeCroy Research Systems Corporation of Spring Valley, New York to NIM standards. Detailed literature on particular units used is available from LeCroy.

a. Beam Logic

The beam logic identified beam pions and provided the proper timing signal whenever a pion was incident on the liquid hydrogen target. The signal CLEAN B_{12} indicated the beam particle entered the hydrogen target and was not accompanied by another in the previous or next 25 nsec. This particle was identified as a pion by the threshold Cerenkov counter C_{π}, which together with CLEAN B_{12} formed the signal BEAM. If, while traversing the target, none of the surrounding anticounters were hit by secondary particles, the signal B was generated and passed to the Slow Arm Logic where particles in the Backward Arm were

identified. The signal BEAM was also put into anticoincidence with the Logic Gate to form the GATED BEAM signal. The GATED BEAM was scaled throughout the experiment and used to normalize the final cross sections. The BEAM signal in coincidence with a pulse generator periodically generated the RANDOM BEAM signal which was used as a diagnostic trigger.

b. Slow Arm Logic

A signal from any S-hodoscope counter indicated a particle in the Backward Arm Spectrometer and after the proper delay was used to stop the appropriate time of flight (TOF) scalar. This, in coincidence with B (to form BS_i) signalled the particle might have come from a beam interaction in the hydrogen target. The individual BS_i signals from each S-hodoscope counters were wired into the FAST-SLOW coincidence matrix, and also OR'ed to form BS. Signal BS was used as a pretrigger to strobe the Multiwire Proportional Chamber (MWPC) latches and pattern units, start the S-hodoscope TOF scalers, and notifiy the Gating Logic that an event was pending. Another diagnostic trigger, Random BS, was also periodically generated by a BS coincidence with a pulse generator.

c. Fast Arm Logic

Refer to figure 20. A particle striking the proper f_α and f_β hodoscope counters formed the signal f_i which was passed into the Fast-Slow coincidence matrix. The matrix compared these signals to the signals BS_i and identified events where the proper combination of hodoscope elements were hit (proper being defined by elastic kinematics). A positive correlation generated the signal BSF. An anticoincidence between BSF and the forward threshold Cerenkov counter, C_F, ensured the forward particle was a proton, and formed the final trigger signal MASTER TRIGGER. Occurance of this signal strobed the remaining MWPC latch and pattern units and initiated the computer readout of the stored information. At the same time, the Logic Gating circuit was signalled that the pending event was a valid trigger.

d. Gating Logic

The Gating Logic (fig. 21) was responsible for controlling the deadtime of the experiment. The arrival of a BS signal set the Logic Gating latch which gated off the beam logic until current event was processed. A delayed BS signal was generated to allow the current event to propagate

through the Fast Arm Logic. The delayed BS in anticoincidence with the MASTER TRIGGER formed the BS RESET. If the delayed BS was not accompanied by a MASTER TRIGGER, a BS RESET signal cleared all latches and reset the Logic Gating latch gating on the beam logic again. If the delayed BS was in coincidence with a MASTER TRIGGER, a BS RESET was not produced and the Logic Gating remained set until reset by computer at the end of the readout cycle.

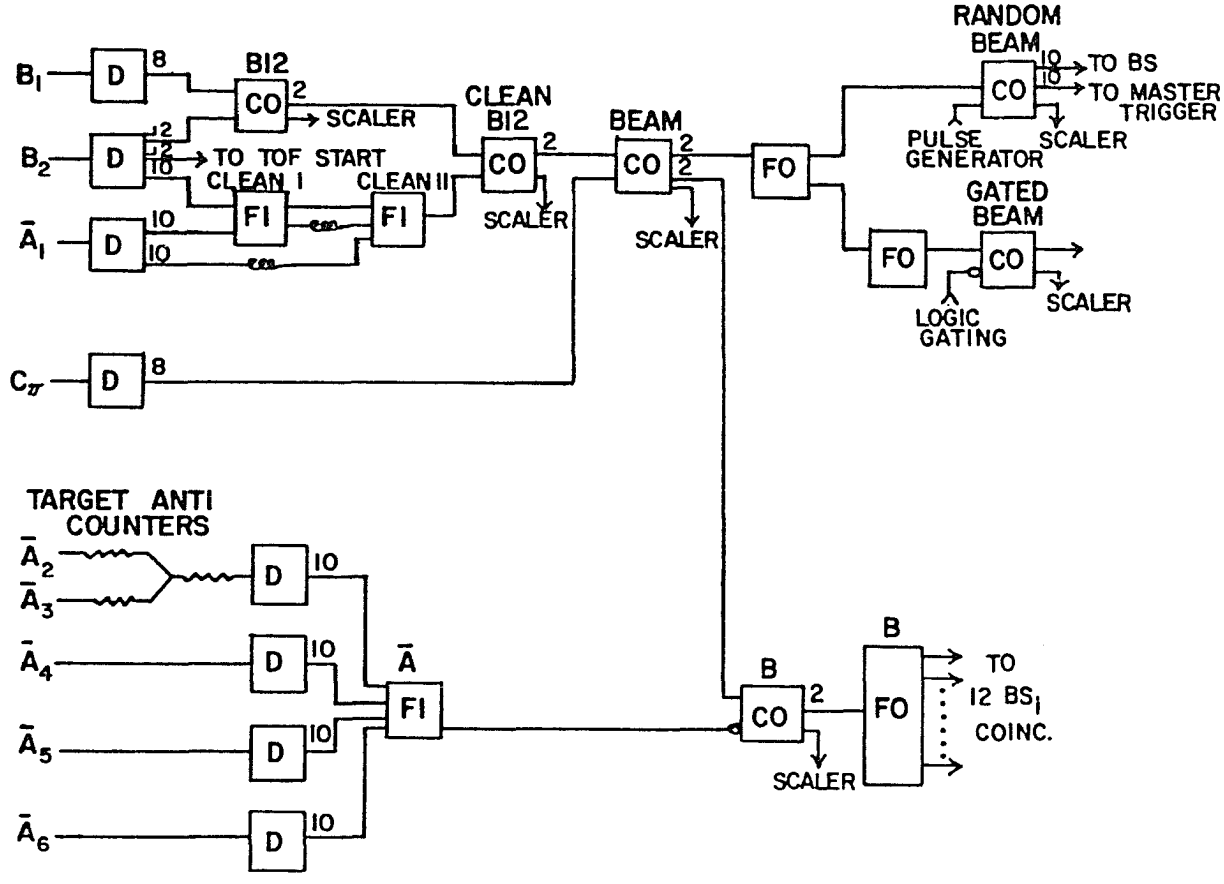

Figure 18. Detailed Diagram of Beam Logic.

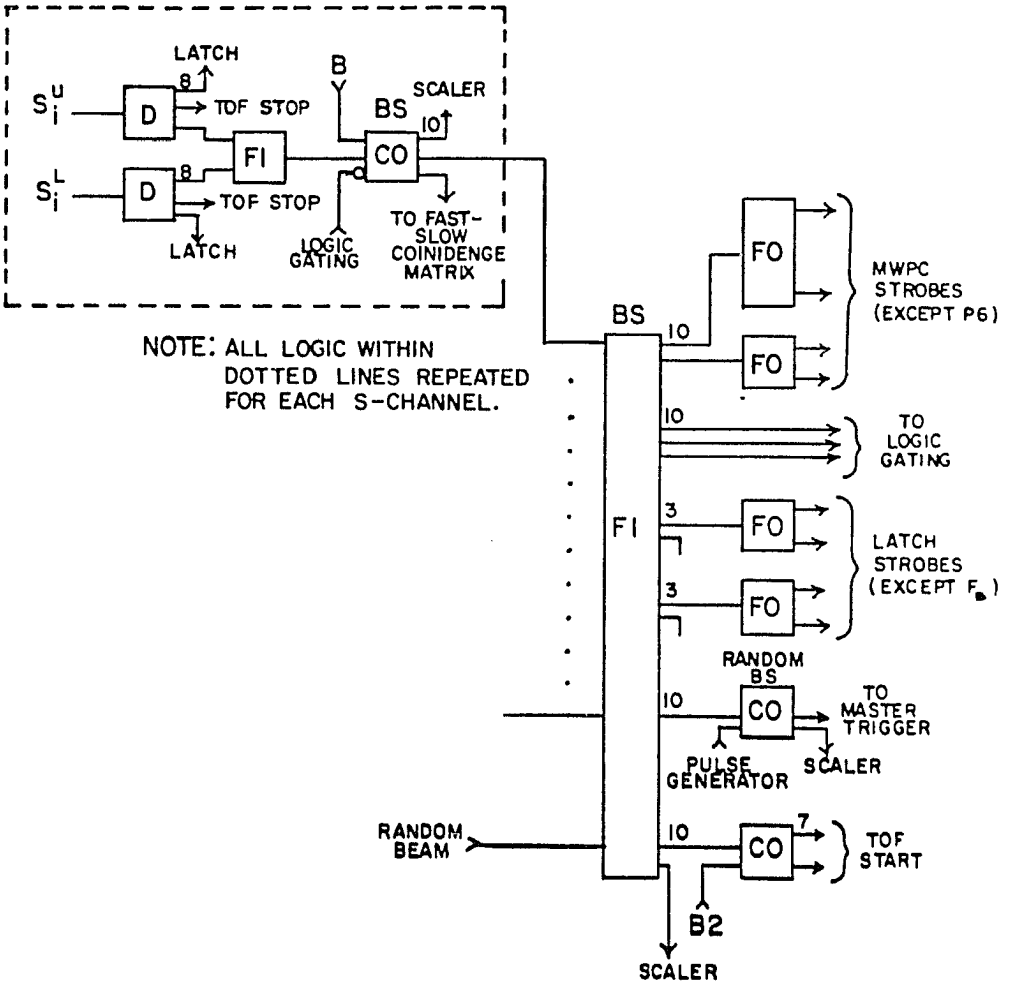

Figure 19. Detailed Diagram of Slow Arm Logic.

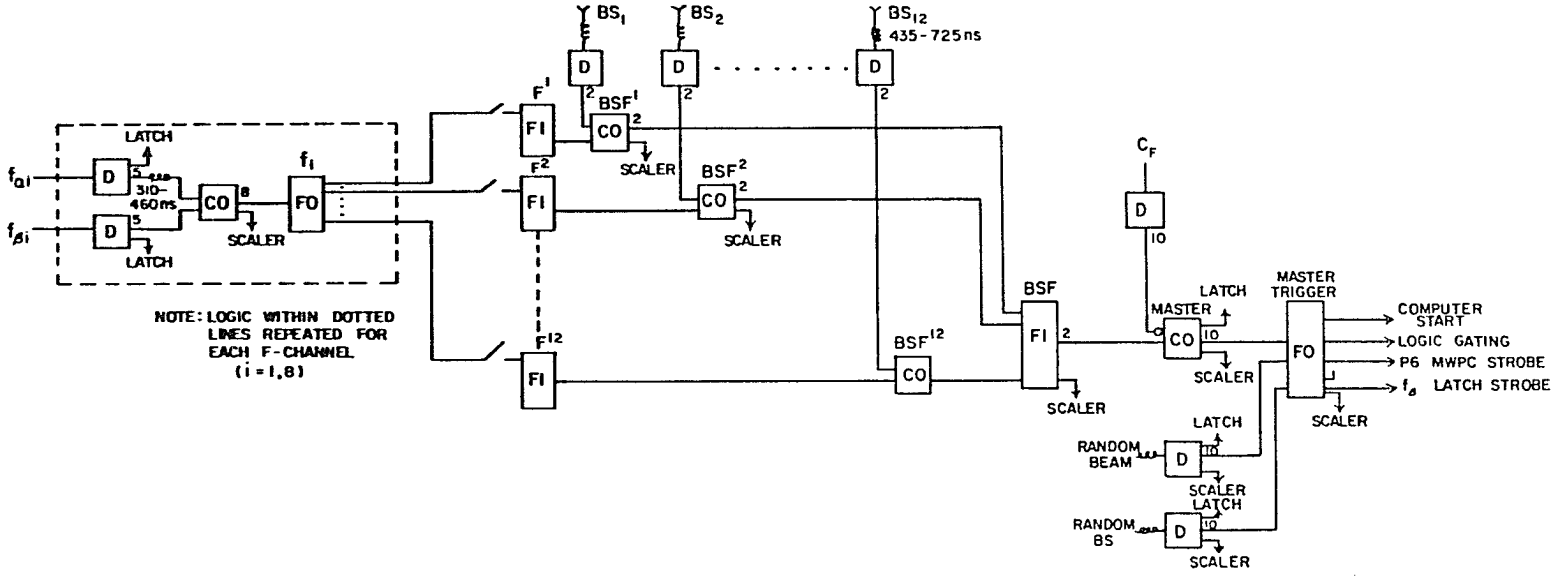

Figure 20. Detailed Diagram of Fast Arm Logic.

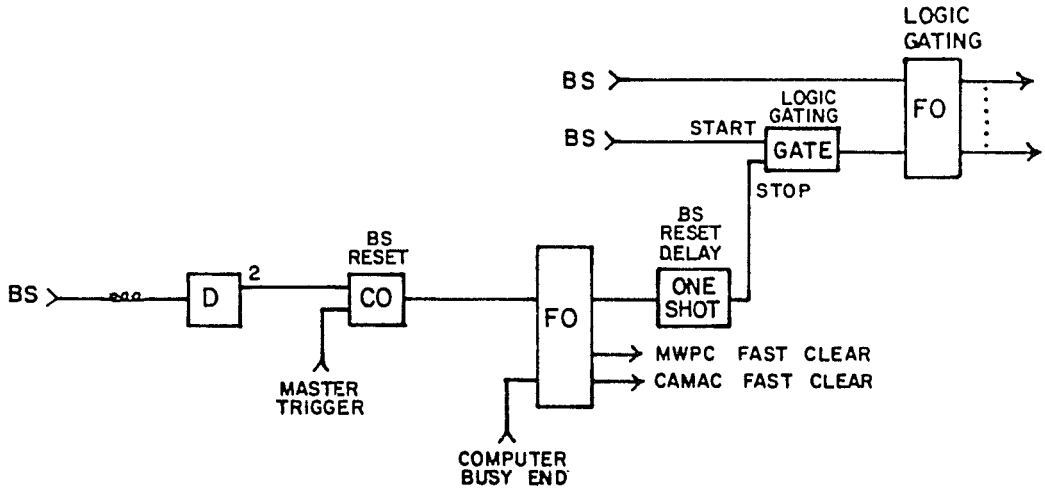

Figure 21. Detailed Diagram of Gating Logic.

REFERENCES

1. Aachen-Berlin-Birmingham-Bonn-Hamburg-London(I.C.)-Munchen Collaboration, Phys. Lett. 10 (1964) 248.

2. Orear, J., R. Rubinstein, D. Scarl, D. White, A. Krisch, W. Frisken, A. Read and H. Ruderman, Phys. Rev. 152 (1966) 1162.

3. Anderson, E., E. Bleser, H. Blieden, G. Collins, D. Garelick, J. Menes, F. Turkot, D. Birnbaum, R. Edelstein, N. Hien, T. McMahon, J. Mucci and J. Russ, Phys. Lett. 20 (1968) 1529.

4. Owen, D., F. Peterson, J. Orear, A. Read, D. Ryan, D. White, A. Ashmore, D. Damerell, W. Frisken and R. Rubinstein, Phys. Rev. 181 (1969) 1794.

5. Baker, W., K. Berkelman, P. Carlson, G. Fisher, P. Fleury, D. Hartill, R. Kalbach, A. Lundby, S. Muhkin, R. Nierhaus, K. Pretzl and J. Woulds, Nucl. Phys. B25 (1971) 385.

6. Lennox, A., J. Poirier, C. Rey, O. Sander, W. Baker, D. Eartly, K. Pretzl, S. Pruss and A. Wehmann, Phys. Rev. D11 (1975) 1777.

7. Jacholkowski, A., B. Bouquet, B. D'Almagne, A. Ferrer, A. Lahellec, P. Petroff, F. Richard, P. Roudeau, J. Six, D. Treille, P. Rivet, P. Benkheiri, P. Fleury, G. DeRosny, A. Rouge and H. Yoshida, Nucl. Phys. B126 (1977) 1.

8. Stein, N., R. Edelstein, D. Green, H. Halpern, E. Makuchowski, J. Russ, D. Weintraub, Z. Bar-Yam, J. Dowd, W. Kern, J. Russell, N. Sharfman and M. Singer, Phys. Rev. Lett. 39 (1977) 378.

9. Sharfman, N., Z. Bar-Yam, J. Dowd, W. Kern, J. Russell, M. Singer, R. Edelstein, D. Green, H. Halpern, E. Makuchowski, J. Russ and N. Stein, Phys. Rev. Lett. 40 (1978) 681.

10. For a brief discussion, see M. Derrick, CERN 68-7, Vol. I (1968).

11. Simmons, L., Phys. Rev. Lett. 12 (1964) 229.

12. Chiu, C. and J. Stack, Phys. Rev. 153 (1967) 1575.

13. Barger, V. and D. Cline, Phys. Rev. Lett. 21 (1968) 392.

14. Barger, V., Rev. Mod. Phys. 40 (1969) 129.

15. Barger, V., Phys. Rev. 155 (1967) 1792.

16. Berger, E. and G. Fox, Nucl. Phys. B26 (1971) 1.

17. Storrow, J. and G. Winbow, Nucl. Phys. B53 (1973) 62; Nucl. Phys. B54 (1973) 560; J. Phys. G. 1 (1975) 263.

18. Irving, A. and R. Worden, Phys. Reports 34C (1977) 117.

19. Barger, V., F. Halzen and M. Olsson, Nucl. Phys. B49 (1972) 206.

20. Babaev, A., E. Brakhman, G. Eliseev, A. Ermilov, Yu. Galaktionov, Yu. Gorodkov, V. Kirilyuk, N. Luzhetsky, V. Lyubimov, V. Nagovitzin, V. Nozik, V. Pogidaev, V. Shelelev, E. Shumilov, I. Sidorov, I. Tikhomirov, T. Tsvetkova, and O. Zeldovich, Phys. Lett. 38B (1972) 342.

21. Babaev, A., E. Brakhman, M. Danilov, G. Eliseev, A. Ermilov, Yu. Galaktionov, Yu. Gorodkov, L. Laptin, V. Lyubimov, V. Nagovitzin, V. Plyaskin, V. Shepelev, E. Shumilov, V. Sopov, I. Tikhomirov, T. Tsvetkova and O. Zeldovich, Phys. Lett. 67B (1977) 351.

22. Ginzberg, I. and L. Perkovskij, Sov. J. Nucl. Phys. 17 (1973) 675 and 23 (1976) 120.

23. Diu, B. and P. Tchang, Nuovo Cimento 32A (1976) 185.

24. Lyubimov, V., Sov. Phys. USP. 20 (1977) 691.

25. Rouge, A., G. DeRosny, P. Fleury, B. Eisenstein, P. Briandet, P. Benkheiri, P. Rivet, A. Volte, B. Bouquet, B. D'Almagne, A. Ferrer, A. Jacholkowski, P. Petroff, F. Richard, P. Roudeau, J. Six, D. Treille and H. Yoshida, Phys. Lett. 69B (1977) 115.

26. Benkheiri, P., B. Eisenstein, P. Fleury, G. DeRosny, A. Rouge, T. P. Yiou, H. Yoshida, D. Treille, P. Rivet, A. Volte, B. Bouquet, B. D'Almagne, A. Ferrer, B. Grossetete, A. Jacholkowski, H. Nguyen, P. Petroff, F. Richard, P. Roudeau, and J. Six., Nucl. Phys. B150 (1979) 268.

27. Ferrer, A., B. Bouquet, B. D'Almagne, B. Grossetete, A. Jacholkowski, H. Nguyen, P. Petroff, F. Richard, P. Roudeau, J. Six, H. Yoshida, D. Treille, P. Rivet, A. Volte, P. Benkheiri, G. DeRosny, B. Eisenstein, A. Rouge, and T. P. Yiou, Nucl. Phys. B142 (1978) 77.

28. Sogard, M., Phys. Rev. D9 (1974) 1486.

29. Borie, E., University of Karlsruhe, Report No. TKP 77-6 (1977) (unpublished).

30. Ginzberg, I., G. Kotkin and V. Serbo, Phys. Lett. 80B (1978) 101.

31. Klinger, J., Fermilab Pub. 80/26 (1980) (to be published).